FEATURE ARTICLE

Chemical Reactions of Nitrogen Oxides on the Surface of Oxide, Carbonate, Soot, and Mineral Dust Particles: Implications for the Chemical Balance of the Troposphere

V. H. Grassian*

Departments of Chemistry and Chemical and Biochemical Engineering, and the Center for Global and Regional Environmental Research, The University of Iowa, Iowa City, Iowa 52242

Received: June 5, 2001; In Final Form: November 5, 2001

Particles present in the Earth's atmosphere provide reactive surfaces for potentially important chemistry. The role of heterogeneous reactions of trace atmospheric gases on solid aerosol surfaces present in the troposphere is not well understood. Laboratory investigations can provide a basis for understanding the detailed molecular-level physical chemistry of these atmospheric reactions. Kinetic data measured in the laboratory, along with the information provided by spectroscopic studies, can be incorporated into atmospheric chemistry models in order to gain a greater understanding of how heterogeneous chemistry affects the chemical balance of the troposphere. Laboratory studies of the heterogeneous uptake of nitric acid, HNO_3, on oxide, carbonate and mineral dust particles, and the heterogeneous formation of nitrous acid, HONO, on wetted-SiO_2 and soot particles are highlighted as two examples of important heterogeneous processes in the troposphere.

1. Introduction

With estimated annual emissions of 3000−5000 Tg of particulate matter in the form of soil dust, sea salt, organics, sulfate aerosol, and soot,[1] it is clear that there are large and diverse sources of particle surfaces that can facilitate heterogeneous chemistry in the troposphere. The role that heterogeneous chemistry on the surface of particles present in the troposphere remains an important question. It is known that particulate matter can influence radiative transfer by absorption and scattering of solar and terrestrial radiation, and by changing the optical properties of clouds through modification of the distribution of cloud condensation nuclei (CCN).[2] Much less is known regarding the role of particular matter as reactive surfaces in the troposphere. However, understanding the chemical interactions between the gas and the aerosol phases is important because these processes may result in a change in the gas-phase chemical composition of the troposphere as well as a change in aerosol composition and size distribution, and thus alter aerosol optical properties.

Because ozone is not directly emitted into the atmosphere but is instead formed by a complex set of photochemical reactions involving nonlinear interactions of NO_x ($NO_x = NO + NO_2$) and volatile organic compounds (VOCs), there is increased interest in heterogeneous chemistry involving ozone and its precursors on aerosol surfaces.[3,4,5] An understanding of all processes that control NO_x and VOC concentrations is key to the development of atmospheric chemistry models that can accurately describe tropospheric ozone formation.[6]

As discussed by Ravishankara,[7] the ability to accurately predict the composition of the troposphere will depend on advances in understanding the role of particulate matter in the atmosphere and the extent to which heterogeneous reactions on solids and multiphase reactions in liquid droplets contribute to the chemistry. Stratospheric particles, known as polar stratospheric clouds (PSC's), have been relatively well studied because of their role in converting chlorine containing reservoir compounds into photoactive chlorine-containing compounds that result in stratospheric ozone depletion (see refs 8 and 9 and references therein). A schematic representation of some of the chemistry involved is shown in Figure 1. PSC's are mainly composed of ice and nitric acid trihydrate (NAT).[8,9] The troposphere, in contrast, has a much higher particle density and a much greater diversity in the types of particles present relative to the stratosphere. Some of the particles found in the troposphere are listed in Figure 1 along with the potential role that they may play. The heterogeneous chemistry of sea salt with trace atmospheric gases has received a fair amount of attention because of the release of reactive chlorine-containing compounds that occurs with many of these reactions. The reader is referred to a recent Feature Article written by Finlayson-Pitts and Hemminger on the heterogeneous chemistry of sea salt and its components.[10]

The motivation for the studies described herein is the recognition that the photochemical oxidant cycle can be altered through heterogeneous uptake and subsequent reactions of atmospheric gases on solid particle surfaces present in the global troposphere. Figure 2 depicts a portion of the photochemical cycle and some potential reactions of trace atmospheric gases on solid aerosols that may be of importance in the chemical balance of the troposphere. A majority of the work in our laboratory has focused on delineating the potential importance of reactions of trace atmospheric gases on mineral aerosol. Mineral aerosol comes in the form of wind-blown soils and is an important component of the earth-atmosphere system. It is estimated that 1000 to 3000 Tg of mineral aerosol are emitted annually into the atmosphere.[1] The emissions of mineral aerosol

10.1021/jp012139h CCC: $22.00
Published on Web 01/19/2002

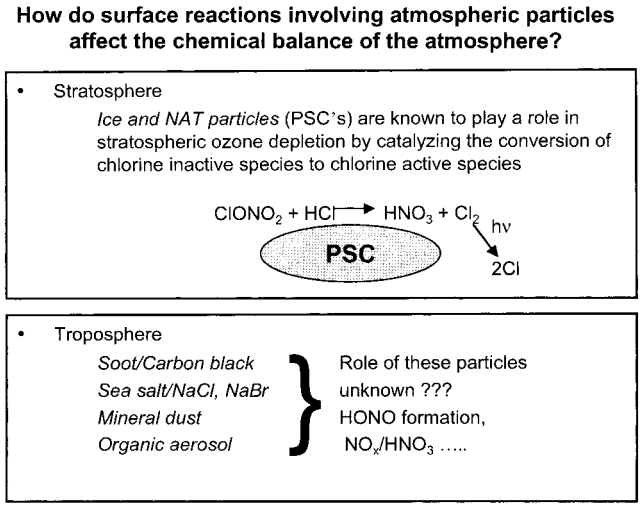

Figure 1. In the stratosphere, photochemically inactive chlorine species, such as chlorine nitrate and hydrogen chloride are converted to photochemically active chlorine species, such as molecular chlorine, on the surface of polar stratospheric clouds (PSC's), such as ice and nitric acid trihydrate (NAT). In the troposphere, there are many different types of particles including sea salt, mineral dust, soot, and organic aerosol, yet little is known about their role in atmospheric chemistry. It has been postulated that these particles may play a role in HONO production and in understanding the discrepancy in the NO_x/HNO_3 ratio measured in field studies but poorly predicted in atmospheric chemistry models that only incorporate gas-phase processes.

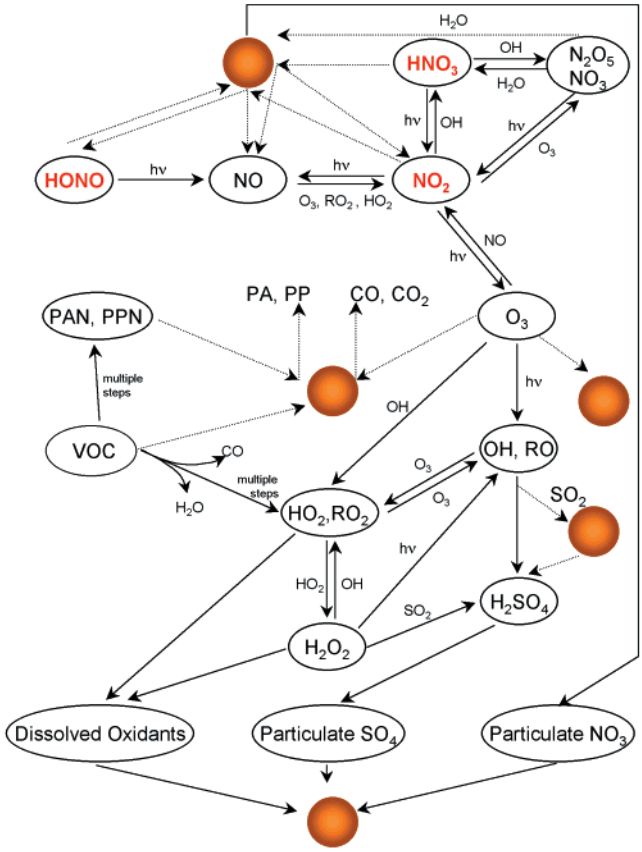

Figure 2. Portion of the photochemical cycle is depicted with known gas-phase chemistry and includes potential reactions of trace atmospheric gases on solid aerosol surfaces (represented by shaded circles): PA, peroxy acetyl radical; PAN, peroxyacetyl nitrate; PP, peroxypropionyl radical; PPN, peroxypropionyl nitrate.

may be increasing substantially as the arid and semiarid areas expand due to shifting precipitation patterns and changes in land use associated with overgrazing, erosion, land salinization, and mining/industrial activities.[11] The importance of mineral dust interactions on tropospheric chemistry has been the subject of several modeling studies.[12−15] Dentener et al. investigated the impact of irreversible reactions of HNO_3, N_2O_5, NO_3, HO_2, O_3, and SO_y on mineral dust surfaces.[13] The results from the modeling study indicate that mineral aerosol may have a significant impact on the chemistry of the troposphere. However, the surface chemistry of mineral aerosol is an area of research that has yet to be fully explored. Mineral aerosols are composed, in part, of metallic and nonmetallic oxides, namely silicates and aluminum silicates, as well as other oxides (e.g., hematite) and carbonates, to list a few examples. In our studies, we have used oxide and carbonate particles as laboratory models for mineral dust found in the troposphere.[16]

As discussed here, laboratory studies coupled with atmospheric chemistry modeling analysis are vital to answering questions regarding the reactive role of solid aerosol in the troposphere. Two examples are discussed here. These include the heterogeneous uptake of nitric acid on oxide, carbonate, and mineral dust particles and the heterogeneous formation of nitrous acid on wetted-silica and soot particles. As will be shown, the heterogeneous uptake of nitric acid by mineral dust provides an important sink for nitric acid and the heterogeneous conversion of one gas-phase species into another, NO_2 to HONO, may be the source of HONO buildup at night. Insights into these heterogeneous reactions gleaned from our work are summarized in this Feature Article.

2. Experimental Methods and Data Analysis

The laboratory studies discussed here are done on solid particles in the powdered form and not suspended as aerosol. Detailed information about the surface chemistry and the adsorption process of trace atmospheric gases on atmospherically relevant solids is derived from the laboratory measurements. The experimental methods include transmission FT-IR spectroscopy, diffuse reflectance UV−Vis spectroscopy and transmission electron microscopy coupled with X-ray microanalysis. Kinetic measurements have been made with several techniques. A Knudsen cell reaction chamber coupled to a quadrupole mass spectrometer is used to measure uptake on powdered samples under dry conditions and to quantify reaction products. The rate of formation of surface-bound products as a function of relative humidity is measured using FT-IR spectroscopy in order to delineate the role of adsorbed water in the heterogeneous reaction kinetics. The experimental techniques used are quite complementary and allow us to probe the solid and the gas phase, so that a complete understanding of the reactants, products and intermediates on the surface and in the gas phase may be obtained. A very important consideration is the surface area of the particles and this quantity is determined with a multipoint-BET apparatus using molecular nitrogen as the adsorbate. Surface areas of all powdered samples used in these experiments, including authentic dust samples and freshly prepared soot samples, have been measured in our laboratory. A summary of the properties of the powders used in these studies is given in Table 1. The details of the laboratory experiments and data analysis are described below.

Transmission FT-IR Spectroscopy of the Solid Surface and the Gas Phase. In the studies described herein, transmission infrared spectroscopy is used to probe the surface of solid particles including oxides, carbonate, and soot samples after adsorption and reaction of trace atmospheric gases. The infrared cell used in these studies is designed such that spectroscopic measurements could be made of both the gas phase and the

TABLE 1: Commercial Sources and Tabulated Values of the Average Diameters and BET Surface Areas of Oxide Particles and Authentic Dust Samples Used in These Studies

sample	source	diameter (cm)	S_{BET} (cm^2/mg)
α-Al_2O_3	Aesar	1.0×10^{-4}	140
γ-Al_2O_3	Degussa	1.8×10^{-6}	1010
α-Fe_2O_3	Aldrich	6.9×10^{-5}	23
γ-Fe_2O_3	Aesar	2.3×10^{-6}	500
TiO_2	Degussa	2.5×10^{-6}	500
SiO_2	Degussa	4.0×10^{-6}	500
MgO	Aesar	1.0×10^{-4}	150
CaO	Aesar	1.3×10^{-4}	39
$CaCO_3$	Aldrich	3.5×10^{-4}	6
Gobi Dust	[a]	4.0×10^{-4}	110
Saharan Sand	[b]	2.5×10^{-2}	31
Hexane Soot	[c]	3.9×10^{-6}	760

[a] Nishikawa M., National Institute for Environmental Studies, Tsukuba, Ibaraki, Japan. Chemical composition from X-ray microanalysis (excluding carbon and oxygen): 48% Si, 22% Ca, 10% Fe, 10% Al, 7% K, 2% Mg, and 1% Ti. [b] Galy-Lacaux C., Laboratory of Aerology, Observatory Midi-Pyrenes, Toulouse, France. Chemical composition from X-ray microanalysis (excluding carbon and oxygen): 80% Si, 1% Ca, 7% Fe, 8% Al, 2% K, 1% Mg, and 1% Ti. [c] Hexane soot was prepared from a flame.

surface (Figure 3) and thus can provide a complete spectroscopic picture of the two important phases under investigation. This is accomplished by coating the powder onto half of a tungsten grid leaving the other half of the grid blank so that gas-phase measurements can be made. Depending on the size, the chemical composition, or the porosity of the powder, samples are coated onto the grid in slightly different ways. The powder can be evenly coated by spraying a water slurry of the particles with an atomizer onto a slightly heated tungsten grid, by painting a paste of the powder onto the grid, or by pressing the powder into the holes of the grid. In the case of freshly prepared hexane-soot, the soot is directly deposited from the flame onto the grid.

The tungsten grid, half-covered with the sample, is then mounted in the IR cell. A schematic of the IR cell is shown in Figure 3. The cell consists of a stainless steel cube with two differentially pumped infrared windows made of BaF_2 and a set of Ni jaws attached to a Ni feedthrough. The tungsten grid is held in place by the Ni jaws and can be resistively heated or cooled by flowing a coolant through the dewar to which the Ni feedthrough is attached. The temperature of the sample is monitored by spot welding thermocouple wires to the center of the grid.

The IR cell is seated on a linear translator inside the FT-IR spectrometer so that both halves of the grid could be measured by simply moving the IR cell through the infrared beam path. The positions of the linear translator and the size of the infrared beam (via a computer-controlled variable iris) are adjusted such that the beam only interrogates each half of the grid. Infrared spectra are recorded with a Mattson RS-10000 spectrometer equipped with a narrowband MCT detector and water-cooled infrared source. Typically, 250 or 500 scans are acquired at an instrument resolution of 4 cm^{-1}. The low-frequency cutoff of the spectrometer is near 750 cm^{-1} due to the detector window.

The entire IR cell is attached to a vacuum chamber through a bellows hose. The vacuum chamber consists of a turbomolecular pump, 80 L s^{-1} ion pump, two absolute pressure transducers for accurate pressure measurements in the 0.001 to 1000 Torr range and a manifold for gas introduction. After the tungsten grid is placed into the IR cell, the system is evacuated to a pressure of 1×10^{-6} Torr. In some cases, it is necessary to heat the particles under vacuum to remove adsorbed water and carbonaceous deposits such as adsorbed carbonate or hydrocarbon impurities from the sample.

The IR cell and gas-handling system described above can be used for experiments involving nitrogen dioxide. Nitric acid decomposes on the walls of the stainless steel reactor so for these studies, the stainless steel cube and the jaws are both Teflon coated. The Teflon-coated jaws are attached directly to the top flange of the cube so that the grid cannot be heated or cooled (see Figure 3). The gas handling system for the nitric acid experiments is completely made from glass and Teflon tubing. Infrared windows made of germanium are found to be less reactive with nitric acid and are used in place of the BaF_2 windows.

Knudsen Cell Measurements: Experimental Apparatus and Data Analysis. The use of the Knudsen cell, a very low-pressure flow reactor, to obtain kinetic information for heterogeneous gas−solid and gas−liquid reactions was pioneered over 30 years ago by Golden, Spokes, and Benson.[17] The general design of Knudsen cell reactors for the study of heterogeneous reactions has been described in detail in the literature.[17−19] Typically, the reactor consists of a chamber with an isolated sample compartment and a small aperture through which gas-phase reactant and product species can escape to be detected, usually by mass spectrometry. Choice of the size of the aperture (or hole), A_h, and the volume of the reactor, V, determine the escape constant, k_{esc}, (i.e., the first-order rate constant), through the cell, as shown in eq 1

$$k_{esc} = \frac{\bar{c} A_h}{4V} \tag{1}$$

where $\bar{c}$ is the average molecular speed of the gas molecules. The residence time of the gas-phase molecules in the Knudsen cell reactor, τ, is defined as the inverse of k_{esc}.

For many of the experiments done in our laboratory, a multi-sample Knudsen cell reactor is used to measure heterogeneous reaction kinetics. A schematic of the reaction chamber of the multi-sample Knudsen cell is shown in Figure 4. A stainless steel reducing cross (6"−2.75") has four individual sample holders attached to a platform that rests on the bottom of a 6" flange. All exposed interior surfaces are coated with Teflon to provide a chemically inert surface. Four Teflon-coated aluminum disks attached to four linear translators serve as covers for each of the powdered samples. The geometric area of each of the four sample holders, A_s, is 5.07 cm^2. Since the volume of the sample holder is only about 2.5 cm^3 and the total volume is near 1500 cm^3, no corrections are needed to account for volume change upon opening the sample compartment. The seal between the sample holders and the cover is made with viton o-rings. With this setup, four different samples are analyzed in a single run. Escape constants between 0.05 and 0.50 s^{-1} are used in these experiments.

The multi-sample Knudsen cell reactor is also coupled to a quadrupole mass spectrometer (UTI, DetecTorr II). The mass spectrometer is housed in a vacuum chamber equipped with a 400 L/s ion pump and an ion gauge (both from Varian). The region between the quadrupole mass spectrometer and the Knudsen cell reactor is pumped by a 150 L/s turbomolecular pump (Leybold) for differential pumping of the mass spectrometer. For all Knudsen cell experiments, flowing the reactive gas through the reactor for at least ninety minutes prior to the experiment passivated the walls of the reactor. The gas was introduced through a leak valve to the desired pressure as measured with an absolute pressure transducer (MKS 690A.1TRC

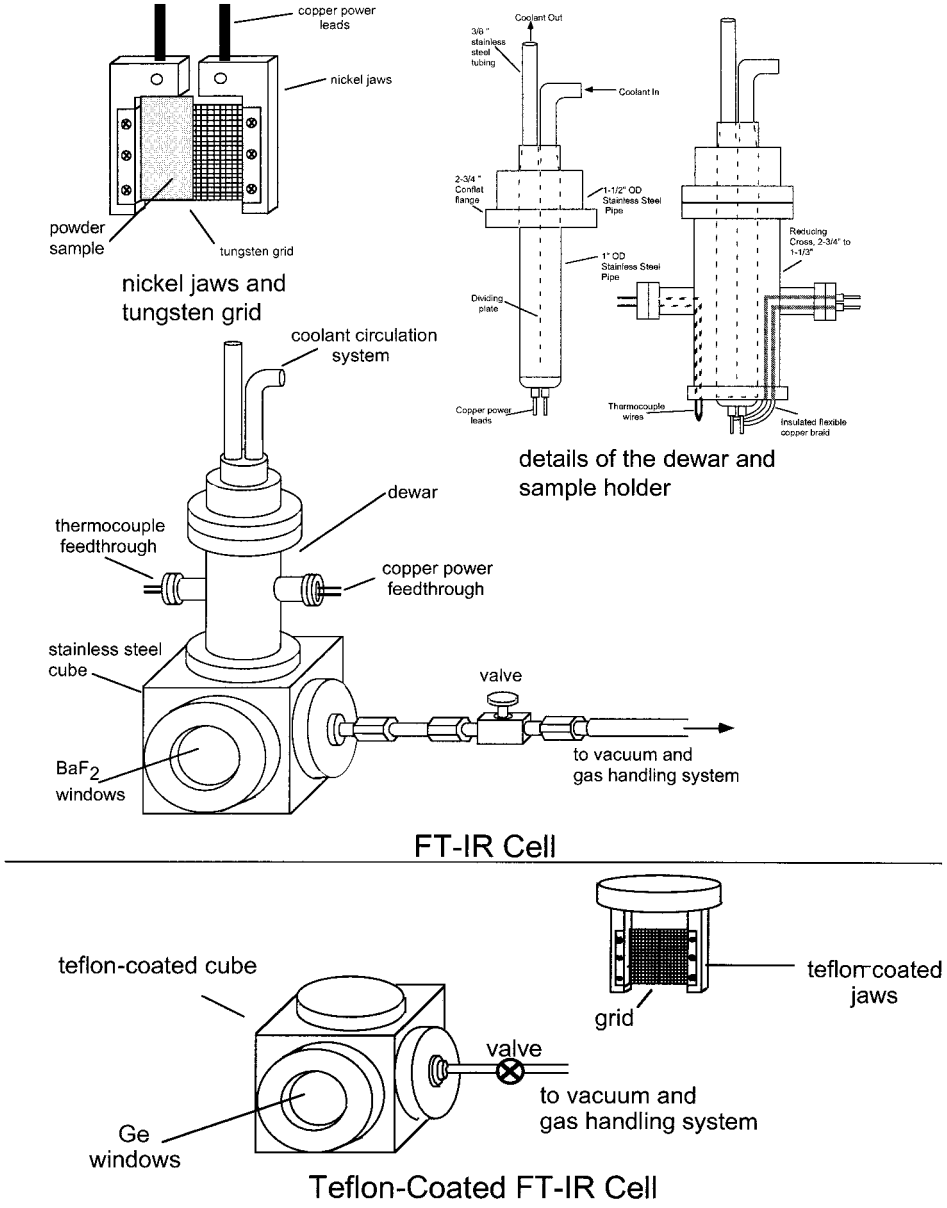

Figure 3. Schematic of the FT-IR cell and other components used to measure the infrared spectrum of surface-bound and gas-phase species. For experiments with nitric acid, a Teflon-coated FT-IR cell was used.

range $10^{-6}-0.1$ Torr). During passivation, the powdered samples were sealed with the Teflon-coated covers.

Samples for the Knudsen cell were prepared in one of two ways depending on how much sample was required for the experiment. For relatively large amounts of sample, typically 0.5−2.0 g, the powdered sample was spread evenly across the sample holder then lightly pressed down to form a flat surface. When much less sample, approximately 2−100 mg, was needed, the powder was sprayed onto the sample holder. It is very important for thin samples that the powdered sample be evenly applied and it must cover the entire geometric area of the sample holder; otherwise the initial uptake coefficient may reflect the amount of uncovered/unreactive surface in the sample holder as well as the sample mass. Both of these concerns are addressed by using an atomizer to spray an aqueous slurry of the sample onto a heated sample holder. This spraying procedure ensured very even coverages of the powdered sample across the bottom of the sample holder, as determined with an optical microscope.

It is useful to determine a heterogeneous uptake coefficient with a Knudsen cell reactor. The heterogeneous uptake coef-

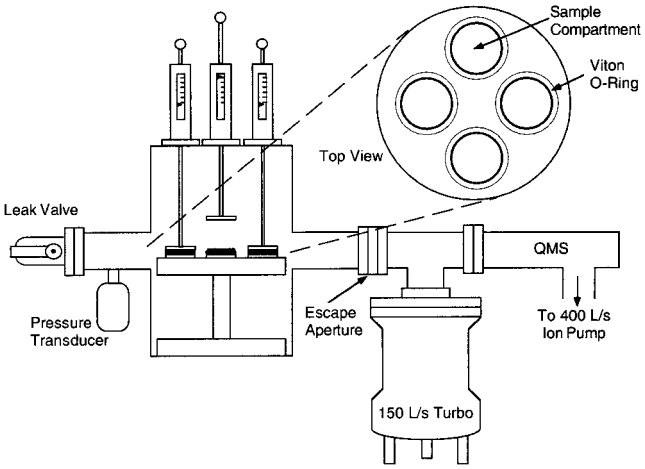

Figure 4. Schematic of the multi-sample Knudsen cell reactor used to measure heterogeneous uptake kinetics of NO_2 and HNO_3 on oxide particles and authentic dust samples.

ficient, γ, is simply a measure of how likely the molecule will be taken up by the surface, through either adsorption or reaction, on a per collision basis

$$\gamma = \frac{\text{the number of molecules taken up on the surface per second}}{\text{the total number of gas - surface collisions per second}} \quad (2)$$

Knudsen cells can be designed so that there is minimal volume change when the sample compartment is opened. In addition, because the flow of molecules into the cell does not change when the sample compartment is opened, the number of the reactant molecules that are "lost" to the surface is equal to the change in flow out of the cell, $(F_o - F)$, where F_o and F represent the gas-phase flow out of the cell with the powdered sample covered and exposed, respectively. It is possible to show that the heterogeneous uptake coefficient, derived under steady-state conditions,[17−19] is defined by eq 3

$$\gamma = \frac{A_h}{A_s}\cdot\left(\frac{F_o - F}{F}\right) \quad (3)$$

where A_h and A_s are defined as the geometric area of the escape hole or aperature and the sample holder, respectively. Because the measured quantity is usually the mass spectral intensity of the reactant gas and this value is directly proportional to the flow out of the cell, eq 3 usually appears as

$$\gamma = \frac{A_h}{A_s}\cdot\left(\frac{I_o - I}{I}\right) \quad (4)$$

Here, I_o and I are the mass spectral intensities measured with the sample covered and exposed, respectively. For reasons described below, the uptake coefficient calculated using eqs 4 and 5 will be referred to as the observed uptake coefficient, γ_{obs}.

It is important to note that in the derivation of eq 3, the total number of gas−surface collisions is taken as the number of collisions that occur with the geometric area of the sample holder. Thus, it is assumed that as the gas molecule approaches the sample, it collides only once and only with the top layer. If the sample were a liquid or a single crystal or even a porous sample with an uptake coefficient approaching unity, this assumption probably would not introduce any substantial error. For powdered samples with uptake coefficients much less than unity, both of these assumptions are clearly oversimplifications whose effects must be carefully considered if true uptake coefficients are to be extracted from the data. However, correcting the observed uptake coefficient, in particular the initial uptake coefficient, for this increased surface area requires an understanding as to how much of the powdered sample is probed by the gas phase during the time scale of the measurement.

In 1991, Keyser, Moore, and Leu (KML) adapted a model from the heterogeneous catalysis literature[21] to explain heterogeneous reactions of atmospheric relevance.[22] The model takes into account gas diffusion into the underlying layers of a porous sample by considering the surface area contribution from both the first layer (external) and underlying layers (internal) of particles in determining uptake coefficients. As the earlier work includes a complete set of justifications and derivations[21,22] that has been summarized in other publications,[23,24] the details will not be presented here. The premise of the model is that the true uptake coefficient, γ_t, can be thought of in terms of external and internal components (see Figure 5), which are related to

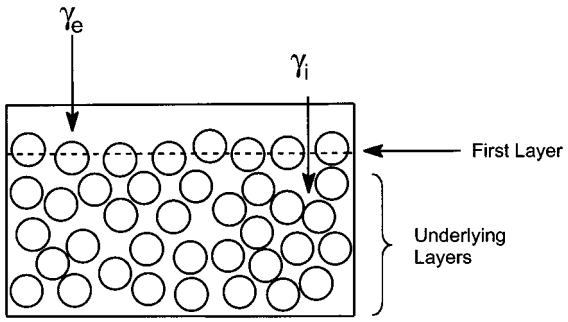

Figure 5. Graphical representation of a powdered sample in the sample holder compartment. External and internal contributions to γ_{obs} are indicated by γ_e and γ_i, respectively. Because the sample holder is of fixed geometry, increasing the mass of the sample increases the sample thickness and thus the number of layers of particles.

the observed uptake coefficient, γ_{obs} by the following equation

$$\gamma_{obs} = \gamma_t\cdot\left(\frac{S_e + \eta\cdot S_i}{A_s}\right) \quad (5)$$

where

$$\eta = \frac{1}{\phi}\cdot\tanh(\phi)$$

and

$$\phi = \left(\frac{m}{\rho_b\cdot A_s\cdot d}\right)\cdot\left(\frac{3\cdot\rho_b}{2\cdot(\rho_t - \rho_b)}\right)\cdot(3\cdot\tau\cdot\gamma_t)^{1/2}$$

The parenthetic term is a correction factor for the effect of gas-phase diffusion into the underlying layers. S_i and S_e are the internal and external surface areas, A_s is the geometric area of the sample holder, and η is a calculated 'effectiveness factor'. The effectiveness factor is the fraction of the internal area that contributes to the measured value of the uptake coefficient. Its value is mass (sample thickness) dependent and is determined from the relative rates of surface adsorption and diffusion into the underlying layers. Because of inhomogenieties in the interparticle voids, however, the effective diffusion constant is less than it would be if calculated assuming diffusion through long straight capillaries. This effect is accounted for by incorporating a tortuosity factor, τ. Porous solids have predicted τ values in the range of 1−8. However most porous solids, especially powders, are not characterized well enough for an accurate calculation of τ to be made, thus, τ must be experimentally determined. The mass, m, geometric area, A_s, particle diameter, d, the true density of the material, ρ_t, and the bulk density of the powder, ρ_b, also contribute to the calculated effectiveness factor.

The form of the equation that we use in our studies is somewhat modified from the work by others in that we do not assume either simple cubic or hexagonal close-packing spheres. Instead, the experimentally measured bulk density was used in the calculations. In addition, the specific BET surface area was measured rather than calculated. Rewriting eq 5 in terms of measured bulk density and BET surface area yields

$$\gamma_{obs} = \gamma_t\cdot\rho_b\cdot S_{BET}\cdot(h_e + \eta h_i) \quad (6)$$

where S_{BET} is the specific BET surface area, h_e is the height of the first layer, and h_i is the height of all the internal layers calculated from the total mass, the measured bulk density and the particle mass. Computer simulations of the KML model

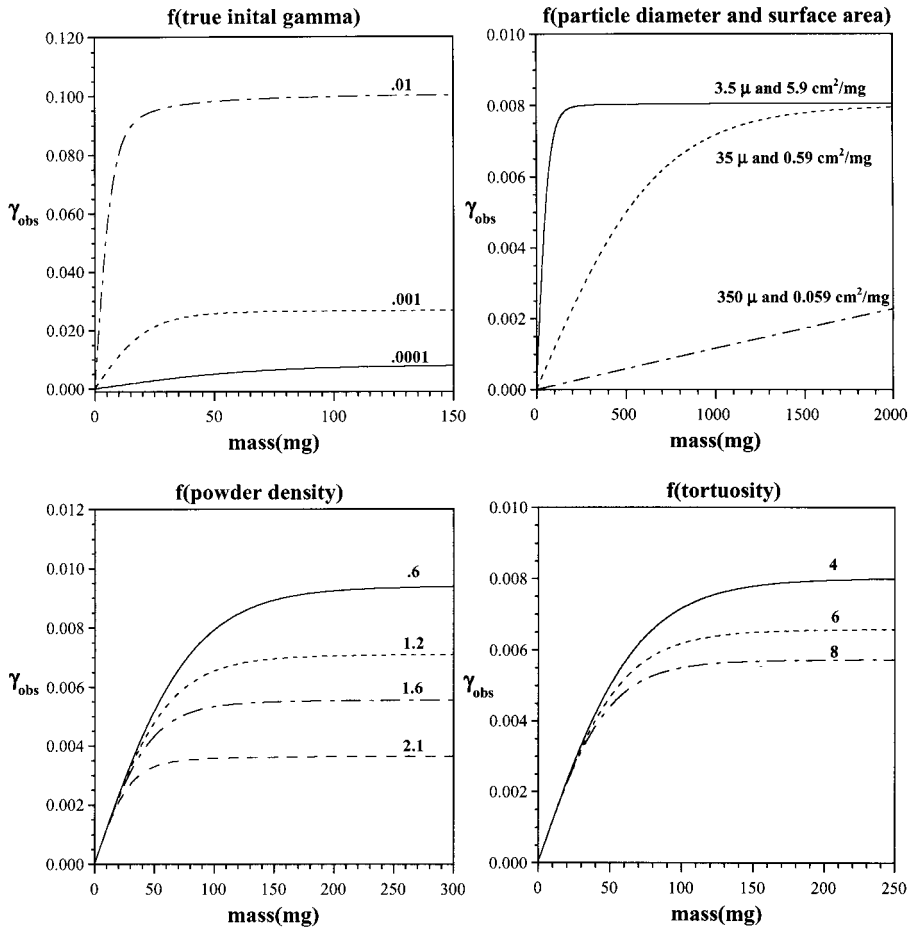

Figure 6. Computer simulations of the γ_{obs} versus mass (or sample thickess) expected for powdered samples. The KML model is used to simulate the γ_{obs} versus mass curves. The simulations show the expected changes in the shape of these curves as a function of gamma, surface area, tortuosity and powder density. Unless otherwise noted, the following parameters are used in the simulation: true initial uptake coefficient, $\gamma_{o,t} = 1 \times 10^{-4}$; tortuosity, $\tau = 2$; the bulk density, $\rho_b = 0.96$ g cm^{-3}; the true density, $\rho_t = 2.93$ g cm^{-3}; the particle diameter, $d = 3.5 \times 10^{-4}$ cm; and the specific BET surface area of the powder, $S_{BET} = 5.9$ cm^2 mg^{-1}.

shown in Figure 6 demonstrate the effect that these different parameters have on the mass dependence of the observed uptake coefficient. Because of the fixed geometry of the sample holder, increasing the mass of the sample increases the sample thickness and thus the number of layers of particles. It can be seen that γ_{obs} is a function of sample mass (i.e., number of layers of particles) in each of the simulations and its value depends on the true uptake coefficient, the size and BET area of the powder, the powder density, and the tortuosity. The parameters used in the model are given in the figure caption.

It is important to note the two regimes evident in these curves. The first regime is seen at low masses. In this regime, the observed initial uptake coefficients has a linear dependence on the sample mass and the number of particle layers. This linear dependence arises because, for very thin samples, the probe or interrogation depth of the reactant gas molecules is greater than the depth of the powdered sample and the entire sample can be accessed on the time scale of the measurement. This time scale is on the order of seconds, as defined by the residence time. In this situation, the entire sample area contributes to the observed uptake coefficient, and extracting the true uptake coefficient from the observed uptake coefficient requires consideration of both the entire reactive area and the resultant increase in the number of collisions a molecule makes within the depth of the powdered sample. As shown below, this leads to a very simple correction factor that will work for any adsorbate/powder system for which this linear mass regime can be measured. The second regime occurs at higher masses and is termed the plateau regime. In the plateau regime, the value of γ_{obs} is independent of sample mass. This independence of sample mass arises because in the plateau regime the gas molecules only diffuse through a portion of the powder on the time scale of the measurement. It is obvious from these curves that when no mass dependence is reported in these types of experiments, it is because the experiments are being done in the plateau region. It can be seen in the simulations that the extent of the linear regime depends on the value of the true uptake coefficient, the particle size and BET area, powder density, and the tortuosity, whereas the slope of the linear regime depends only on the true uptake coefficient and the size and surface area of the particles. These two regimes have been observed in kinetic measurements of the heterogeneous uptake coefficient measured for nitrogen dioxide, nitric acid, sulfur dioxide, and carbonyl compounds on oxide, carbonate, soot, and authentic dust samples.

There is a simple way to determine the true uptake coefficient using a simple correction factor that will work for any gas/powder system in which the linear mass regime can be measured. In the linear region, the incoming molecules can access all of the particles and a correction for the "internal" collisions in the lower layers of the powdered sample must also be found. Equation 7 gives a simple correction factor with which the true uptake coefficient, corrected for multiple collisions with

the entire BET sample area, can be extracted from the observed value, which assumes no diffusion into the underlying layers

$$\gamma_t = \frac{A_h}{A_{BET}}\left(\frac{I_o - I}{I}\right) = \left(\frac{A_s}{A_{BET}}\right)\cdot\gamma_{obs} \quad (7)$$

The correction factor, like the number of collisions, scales with the BET area, A_{BET}.

Typically, the initial uptake coefficient is reported. In most cases, a plot of the initial observed uptake versus mass is used to determine the true uptake coefficient. This is done by determining the slope of the best fit line through the $\gamma_{o,obs}$ versus mass data and then calculating the true initial uptake coefficient, $\gamma_{o,t}$, as follows

$$\gamma_{o,t} = \text{slope } (\text{mg}^{-1})\cdot\frac{A_s\ (\text{cm}^2)}{S_{BET}\ (\text{cm}^2\text{mg}^{-1})} \quad (8)$$

There are some additional complications in measuring heterogeneous reaction kinetics with a Knudsen cell reactor that should be mentioned here.[25] First, the analysis assumes steady-state uptake. As will be shown, the uptake coefficient is not constant but in fact decreases with time as the surface becomes saturated. When surface saturation occurs on the time scale of the measurement, the measured initial uptake coefficient determined using eqs 7 and 8 may in fact be a lower limit. Saturation effects will be important when γ is greater than $\sim 10^{-4}$, at high gas pressures and when there are a small number of surfaces sites.

3. Heterogeneous Uptake of HNO_3 on Carbonate, Oxide, and Mineral Dust Surfaces

As discussed in the Introduction section, heterogeneous reactions that affect the concentration of gas-phase nitrogen oxides have important implications for tropospheric chemistry. Consequently, an understanding of processes that control NO_x concentrations is key to the development of models that can accurately describe tropospheric ozone. One problem encountered by present modeling efforts that rely on gas-phase chemical processes alone, is that the calculated HNO_3 to NO_x ratio is typically over-predicted by a factor of 5 to 10.[26−28] Therefore, heterogeneous processes that preferentially remove HNO_3 or recycle NO_x from HNO_3 more efficiently than HNO_3 photolysis or reactions with OH, could potentially reconcile the predictions and the observations.

The impact of irreversible reactions of HNO_3, N_2O_5, NO_3, HO_2, O_3, and SO_y on dust surfaces has been investigated through modeling analysis. The results illustrated that mineral aerosol may have a significant impact on the chemistry of the troposphere.[13] In the case of sulfur, a significant fraction of sulfate is predicted to be associated with mineral aerosol. An even larger fraction of gas-phase nitric acid may be neutralized by mineral aerosol. The regions where at least 40% of the total nitrate is found on the mineral aerosol covers vast regions of the Northern and Southern Hemispheres. During the months of February, March, and April, the region covers almost all of Asia and extends throughout the central and northern regions of the Pacific Ocean basin, and the tropical and sub-tropical Atlantic and Indian Oceans. Only the regions of western and central Europe, the eastern parts of North and Central America, and the high latitude ($>60°$) zones are predicted to have relatively small portions of HNO_3 associated with the mineral aerosol. The effect of dust interactions can be intensified on regional-scales during high dust periods, where surface areas of the mineral aerosol can be an order of magnitude higher than the monthly averaged values calculated by the global model.[14,29]

The model calculations discussed above, whereas extremely valuable in assessing the potential role of heterogeneous reactions on aerosol, remain highly uncertain due to the fact that there is little information on heterogeneous reaction mechanisms and reaction rates.[30] Therefore, it is essential to determine the heterogeneous reaction chemistry of particles present in the troposphere. The heterogeneous reactivity of nitric acid on particles of atmospheric relevance is discussed below. Spectroscopic and kinetic measurements have been made in order to develop a molecular-level understanding of the heterogeneous chemistry of HNO_3 on oxide, carbonate, and mineral dust particles, and the details of the laboratory investigation are then incorporated into an atmospheric chemistry box model for further analysis.

Knudsen Cell Reactor Measurements of HNO_3 Uptake on Oxide, Carbonate, and Mineral Dust. Heterogeneous reaction kinetics of HNO_3 have been measured on Saharan sand, Gobian dust, and six different oxide samples including SiO_2, Al_2O_3, Fe_2O_3, TiO_2, CaO, and MgO. The heterogeneous uptake kinetics for the uptake of HNO_3 on oxides and authentic dust samples was also measured. As discussed above, reaction of HNO_3 at 295 K on most of the oxides appears to be simple adsorption with no detectable gas-phase products. However, reaction with both MgO and CaO appears to produce water. One possible explanation for this is the neutralization reaction

$$MO + 2HNO_3 \rightarrow M(NO_3)_2 + H_2O \quad (9)$$

where M is either Mg^{2+} or Ca^{2+}.

The observed initial uptake coefficients for HNO_3 were measured as a function of sample mass and the true initial uptake coefficients were then determined. Representative Knudsen cell data using the multi-sample holder cell is shown in Figure 7, and both the raw data (a) and the observed uptake as a function of time (b) are plotted. The initial uptake is plotted as a function of sample mass in (c). The plot shows that the observed initial uptake coefficient for HNO_3 on α-Al_2O_3 is linearly dependent on mass for small amounts of the α-Al_2O_3 powder. Plots of $\gamma_{o,obs}$. determined via eq 4, as a function of sample mass were determined for several oxides and the authentic dust samples. For thin sample masses, $\gamma_{o,obs}$ versus mass was found to be linear. The slopes of these plots and values of $\gamma_{o,obs}$ determined using eq 8 are presented in Table 2.

Adsorbed water has also been shown to play an important role in HNO_3 uptake on salt particles.[32,33] Some investigations into the effect of surface water were done in the Knudsen cell reactor. It has been demonstrated by infrared spectroscopy that even after pumping overnight, oxide powders can still retain some adsorbed water. The reactivity of these comparatively "wet" samples were compared to samples which had been heated. The results for CaO and Gobi dust are plotted in Figure 8 where it can be seen that even a small change in the amount of water on the surface can have a significant effect in the uptake coefficient, (a factor of 27 for CaO and 10 for Gobi dust), similar to what is observed in infrared experiments. The role of water in the heterogeneous uptake of nitric acid on oxide and carbonate particles is discussed in more detail in the next section.

Role of Water Vapor and Surface Adsorbed Water in the Heterogeneous Uptake of HNO_3 on Oxide, Carbonate, and Authentic Dust Particles. The role of adsorbed water in the uptake of gases on solid aerosol surfaces is a focus of many

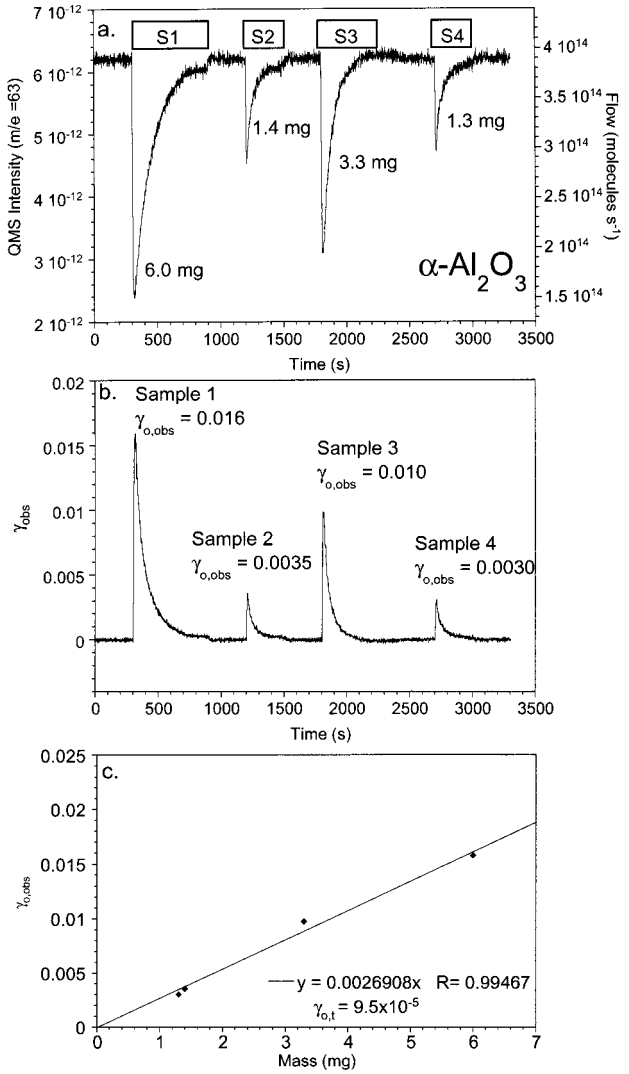

Figure 7. Upper panel: (a) Typical Knudsen cell data for the uptake of nitric acid on four different samples (S1 − S4) of α-Al_2O_3 represented in both QMS intensity ($m/e = 63$) (left axis) and flow (right axis). The rectangular boxes denote the times during which the sample compartments were opened. (b) The uptake coefficients calculated for the data shown in the upper panel using eq 8 with an escape aperture of $A_h = 0.0484$ cm^2 and $A_s = 5.07$ cm^2. The initial pressure in the Knudsen cell is 40 μTorr (1.3×10^{12} molecules/cm^3). (c) Initial uptake coefficient calculated using eq 4 for α-Al_2O_3 as a function of sample mass.

TABLE 2: Experimentally Determined True Initial Uptake Coefficients for the Reaction of HNO_3 with the Oxide Particles and Authentic Dust Samples Used in These Experiments

sample	$\gamma_{o,t}^{a,b}$
α-Al_2O_3	9.7×10^{-5}
SiO_2[c]	2.9×10^{-5}
α-Fe_2O_3	5.3×10^{-5}
MgO	4.0×10^{-4}
CaO	6.1×10^{-3}
$CaCO_3$	2.4×10^{-4}
China Loess	5.2×10^{-5}
Saharan Sand	2.0×10^{-5}

[a] Calculated using eq 8 (see text). [b] All data collected with sample holder area = 5.07 cm^2. [c] Larger SiO_2 particles were used in these experiments with a surface area of 500 cm^2/mg.

studies. Water can play a dual role acting as a reactant, as in the case of the hydrolysis of N_2O_5 to give HNO_3, and as a

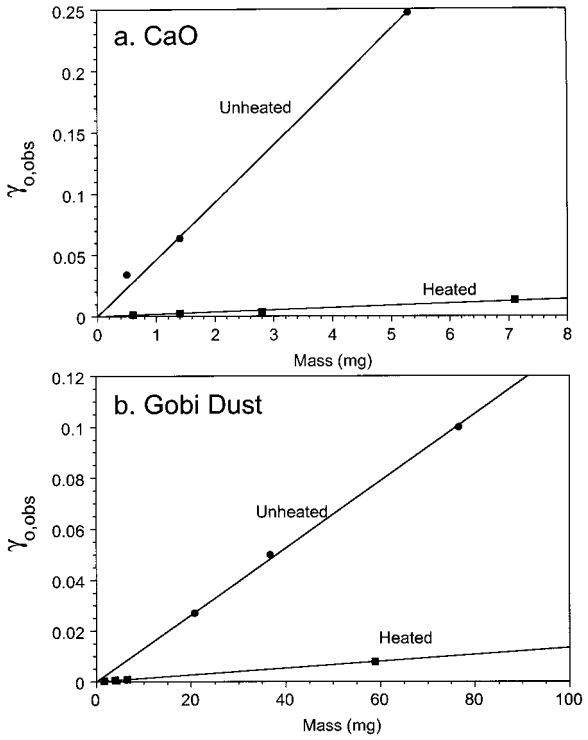

Figure 8. Initial uptake coefficient calculated using eq 4 for unheated and heated samples of both CaO and Gobi dust. The filled circles represent samples that have been evacuated overnight but not heated and thus have a small amount of water adsorbed on the surface. The filled squares depict samples for which much of the water has been removed by heating to 40 °C overnight under vacuum. From the slope of the lines, it is determined that there is a decrease of a factor of 27 and 10 for heated samples of CaO and Gobi dust, respectively.

medium for the ionic dissociation of gases, i.e., inorganic and organic acids can undergo dissociation in aqueous media as follows

$$HA\ (aq) \rightarrow H^+(aq) + A^-\ (aq) \qquad (10)$$

The ionic dissociation reaction will be greatly facilitated by adsorbed water and a "liquid" water layer on the aerosol surface. The hypothesis of a water layer or a quasi-liquid layer is analogous to that discussed by Abbatt et al.[34] and Molina[35] for HCl on ice surfaces in which a "quasi liquid" hydrochloric acid solution with essentially the same chemical reactivity as that of a true liquid HCl solution is formed. Vogt and Finlayson-Pitts also propose a similar picture involving a water layer for the reaction of HNO_3 on NaCl particle surfaces.[36] When water is present, the nitrate ions may be in a quasi-liquid state in which nitrate ions are mobile. Upon heating, the nitrate ions coalesce to form separate regions of $NaNO_3$ on the NaCl surface. Davies and Cox[33] also investigated the heterogeneous reactions of HNO_3 with NaCl in the presence of H_2O vapor. They proposed a two-step process whereby adsorption of HNO_3 molecules on the surface is followed by diffusion to the defect sites where water molecules were adsorbed. They also proposed that bulk reactivity of the NaCl particle was possible as these defect sites were regenerated. Other studies also support the importance of water in HNO_3 uptake on salt.[37−39]

In our laboratory, we have investigated the role that water plays on the uptake of nitric acid on oxide particles, mineral dust, and $CaCO_3$. Our interest in calcium carbonate comes from the suggestion that mineral aerosols containing $CaCO_3$ may be especially effective in removing gas-phase HNO_3 from the

atmosphere, as shown in reaction 11[13,15]

$$CaCO_3(s) + 2HNO_3(g) \rightarrow Ca(NO_3)_2(s) + CO_2(g) + H_2O(g) \quad (11)$$

This heterogeneous pathway may provide a significant chemical sink for HNO_3, especially if the reaction is not limited to the surface of the $CaCO_3$ particle but can react into the bulk of the particle. Song and Carmichael modeled reaction 11 with aerosols containing $CaCO_3$ and found the HNO_3 to NO_x ratio to decrease by a factor of 2 to 6 when compared to models containing only gas-phase processes. Even using the recently measured rate for the oxidation of NO_2 by hydroxyl radicals which is 20−30% lower than previously reported,[40] it is found that heterogeneous loss of HNO_3 is still significant in the modeling results.[41,42] Tabazadeh et al. have also suggested that heterogeneous reactions on biomass aerosols, as well as mineral dust containing $CaCO_3$, can irreversibly remove HNO_3 from the gas phase and provide an important sink for HNO_3.[15] As discussed in detail below, surface adsorbed water, which is a function of the relative humidity, greatly increases the extent and rate of reaction of nitric acid on oxide, carbonate and mineral dust.

In Situ Spectroscopic Measurements of the Heterogeneous Reaction of HNO_3 on $CaCO_3$ Particles in the Presence of Water Vapor. The reaction of gaseous HNO_3 on $CaCO_3$ particles with varying amounts of H_2O has been investigated using FTIR spectroscopy at 295 K. Upon exposure of HNO_3 to dry $CaCO_3$ particles, very little changes in the gas-phase spectrum and that of the solid particle are observed. When $CaCO_3$ is exposed to HNO_3 in the presence of H_2O vapor corresponding to 20% relative humidity (RH), there are several interesting changes in both the infrared spectrum of the gas phase and of the $CaCO_3$ particles. First, in the spectral range extending between 1100 and 750 cm^{-1}, absorption bands at 813 and 1045 cm^{-1} due to adsorbed $Ca(NO_3)_2$ continuously grow in intensity as $CaCO_3$ is exposed to HNO_3 in the presence of H_2O vapor (Figure 9a) and there is no evidence of surface saturation. Second, CO_2 appears in the gas-phase as shown in the inset of Figure 9a. Third, as $CaCO_3$ reacts with HNO_3 to form $Ca(NO_3)_2$, a broad band between 3000 and 3750 cm^{-1} continuously grows in intensity (Figure 9b). This broad band is composed of three peaks at 3280, 3530, and 3605 cm^{-1} which are assigned to the OH stretching vibrations of water adsorbed on the particle surface. As discussed below, this increase in water adsorption at a constant water vapor pressure can be explained by the increase in the amount of $Ca(NO_3)_2$ on the particle surface. Calcium nitrate is approximately 100 times more soluble than calcium carbonate.[43] Therefore, as HNO_3 is reacted with $CaCO_3$ in the presence of water, $CaCO_3$ is converted to $Ca(NO_3)_2$ allowing more water to adsorb onto the surface.

The spectrum of water adsorbed on $CaCO_3$ particles reacted with HNO_3 is distinctly different from the spectrum of adsorbed water on $CaCO_3$ particles not exposed to nitric acid. For example, in the early stages of the reaction when $CaCO_3$ particles are exposed to HNO_3 in the presence of H_2O vapor, the surface water band is first detected as a single asymmetric broad band centered at 3500 cm^{-1}. As the reaction progresses, three distinct peaks at 3605, 3530, and 3280 cm^{-1} within the broad band between 3750 and 3000 cm^{-1} become apparent.

Peters and Ewing (1997) have investigated water adsorption on NaCl(100) under ambient conditions.[44] In their studies, they found that at coverages less than two monolayers, water absorbed on NaCl(100) surfaces behaves similarly to that of condensed water. However, as coverage increases above two monolayers, they found that Na^+ and Cl^- ions incorporate into the water layer, although the water layer does not yet have properties of a bulk salt solution. At coverages greater than three monolayers, the water film has properties of a bulk brine solution. This observation is consistent with the work of Barraclough and Hall,[45] who showed that after adsorption of the first two water layers on NaCl, the H_2O−NaCl isotherms behaved as if a saturated solution of NaCl were present. Other studies provide additional details concerning the interaction of H_2O and salt surfaces.[46−49]

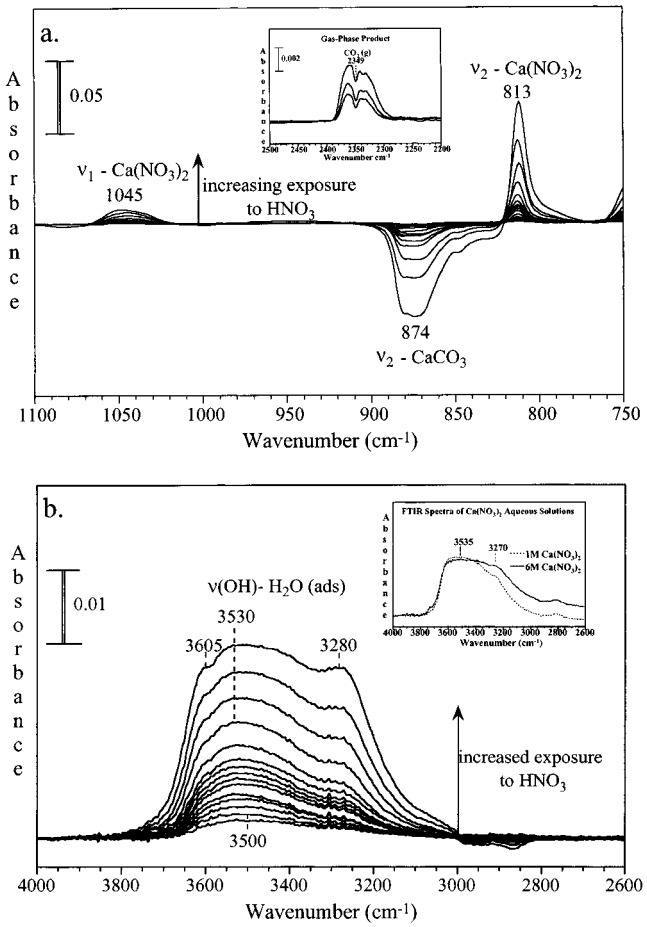

Figure 9. (a) Transmission FT-IR difference spectra of adsorbed products on $CaCO_3$ in the spectral range between 1100 and 750 cm^{-1}. FT-IR spectra of $CaCO_3$ were recorded as a function of HNO_3 exposure (mTorr pressure range) in the presence of gas-phase H_2O (20% RH). The negative features are due to the loss of calcium carbonate and the positive features are due to the growth of calcium nitrate. The inset shows the growth of the absorption band due to the production of gas-phase CO_2 as the reaction proceeds. (b) Transmission FT-IR difference spectra of adsorbed products on $CaCO_3$ in the spectral range between 4000 and 2600 cm^{-1}. FT-IR spectra of $CaCO_3$ were recorded as a function of HNO_3 exposure (mTorr pressure range) in the presence of gas-phase H_2O (20% RH). The infrared data show that as the reaction proceeds there is growth in the infrared absorption band due to adsorbed water on the particle surface. The inset shows the transmission FT-IR spectra of concentrated solutions of $Ca(NO_3)_2$ in water at concentrations of 1 and 6 M. There is similarity between the aqueous solution phase spectra and the spectra of adsorbed water on the nitric acid reacted $CaCO_3$ particles.

The water adsorption spectra shown here on nitric acid reacted $CaCO_3$ can be interpreted in a similar manner. FT-IR spectra of 1 and 6 M $Ca(NO_3)_2$ solutions in the spectral range extending from 2600 to 4000 cm^{-1} are shown in the inset of Figure 9b. In these spectra there is a broad absorption band between 3000 and 3800 cm^{-1} with two bands at 3270 and 3535 cm^{-1} on top of the broad spectrum. Although there is some shift in the

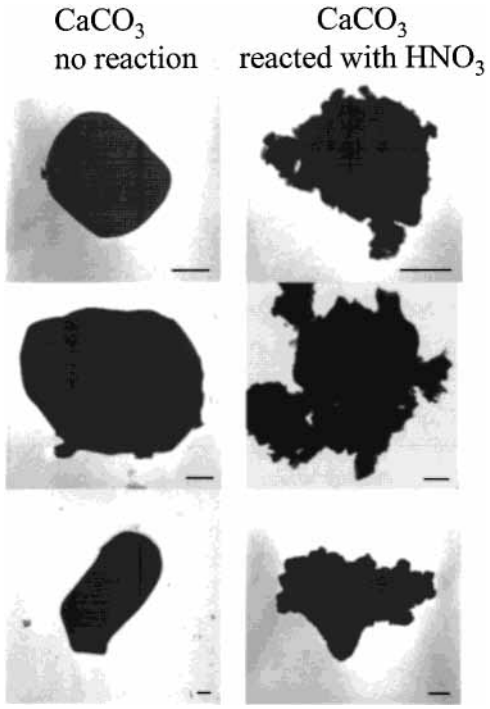

Figure 10. Transmission electron micrographs of calcium carbonate particles that have not been exposed to nitric acid vapor compared to calcium carbonate particles that have been exposed to nitric acid vapor in the presence of water vapor. The particles that have not been exposed are nearly spherical with smooth edges, and the particle surface appears smooth on the one micron length scale (bar = 0.5 μm). In contrast, particles that have been exposed become irregularly shaped with rougher surfaces.

frequency of the bands, the spectra of the $Ca(NO_3)_2$ solutions look very similar to the spectra obtained by exposing H_2O to $CaCO_3$ particles that were reacted with HNO_3. The solution-phase data support that Ca^{2+} and NO_3^- ions are being incorporated into the water film on the $CaCO_3$ particles and are perturbing the hydrogen-bonding network of the water film.

Transmission electron microscopy (TEM) measurements of the $CaCO_3$ particles after reaction of HNO_3 and $CaCO_3$ in the presence of H_2O also provided insight about the particle reactivity. A comparison of the electron micrographs of reacted $CaCO_3$ particles and unreacted $CaCO_3$ particles are shown in Figure 10. The unreacted $CaCO_3$ particles, on the length scale shown in the image, have smooth edges. $CaCO_3$ particles reacted with HNO_3 at a RH of 20% are irregular in shape and have jagged edges. These images show that the smooth edges of the $CaCO_3$ particles become highly irregular in shape after reaction with HNO_3 and thus increase the surface area of the $CaCO_3$ particles. These results are similar to that found for nitric acid uptake on NaCl where microcrystallites of $NaNO_3$ are formed giving rise to changes in particle morphology.[50,51] In light of the similarities between the NaCl and the $CaCO_3$ particle morphology changes upon exposure to HNO_3, the jagged edges observed in the $CaCO_3$ micrographs are most likely of $Ca(NO_3)_2$ microcrystallites.

Several important findings come from the TEM and IR measurements along with gravimetric analysis that has been previously described.[52] First, these experiments show that the nitric acid reaction on $CaCO_3$ is not limited to the surface but can react with the bulk of the particles. This is important as the reactivity is not limited to one layer and a surface coverage of $\sim 5 \times 10^{14}$ molecules cm^{-2}. Second, the uptake of nitric acid on $CaCO_3$ is found to be irreversible. Third, the ability of the particle to adsorb water is greatly enhanced and suggests that a

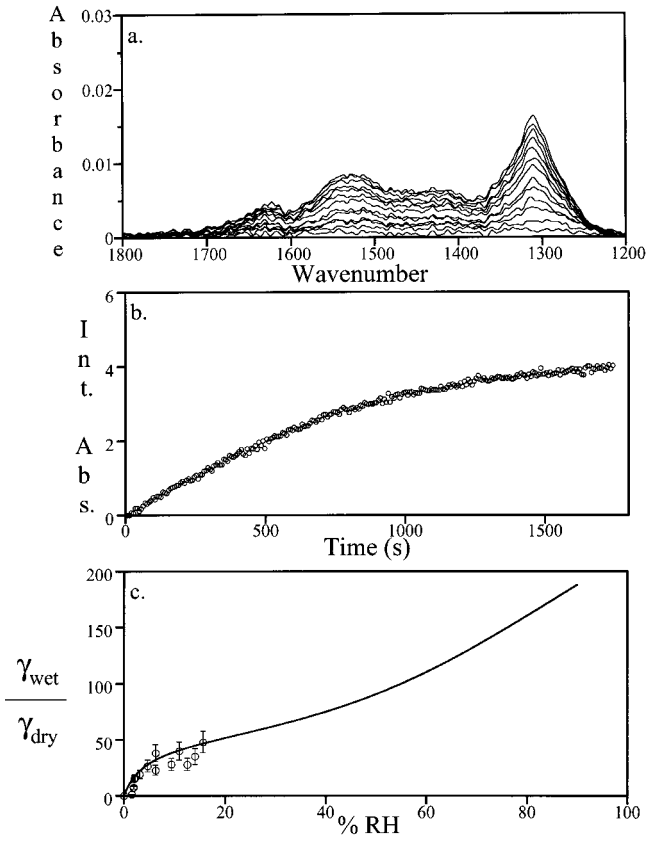

Figure 11. (a) Transmission FT-IR spectra of HNO_3 uptake on α-Al_2O_3 and CaO particles as a function of time. For clarity, only every tenth spectrum collected is shown. (b) The integrated absorbance (or peak height) for the absorption bands of adsorbed nitric acid is plotted as a function of time in the inset. The integrated absorbance of every spectrum collected is plotted. (c) Enhancement of the reactive uptake as a function of relative humidity for HNO_3 uptake on α-Al_2O_3. Open circles represent $\gamma_{wet/dry}$ as a function of relative humidity. The solid lines represent the modified BET isotherm fit for water adsorption on α-Al_2O_3 (see text for further details).

significant water layer will be involved in the subsequent reactivity of the particle.

In Situ Spectroscopic Measurements of the Heterogeneous Reaction of HNO_3 on Oxide Particles in the Presence of Water Vapor. Similar to the irreversible uptake of nitric acid on calcium carbonate particles, nitric acid also irreversibly adsorbs at 295 K on nearly all of the oxides investigated, Al_2O_3, Fe_2O_3, TiO_2, CaO, and MgO, with the exception of SiO_2.[31] Surface limited reactions are observed for Al_2O_3, Fe_2O_3, and TiO_2, whereas for the basic oxides, CaO and MgO, surface and bulk reactivity, similar to that found for $CaCO_3$, are found to occur in the presence of water vapor. The rate of HNO_3 uptake on oxide particles as a function of relative humidity was determined by time course FT-IR experiments.

Representative spectra collected for HNO_3 uptake on α-Al_2O_3 under dry conditions as a function of time are shown in Figure 11a. The α-Al_2O_3 particles were exposed to 9 mTorr of HNO_3 corresponding to 2.9×10^{14} molecules cm^{-3} and spectra were then recorded as a function of time. The extent of nitric acid uptake on α-Al_2O_3 was determined by integrating the absorptions in the region 1189−1822 cm^{-1}. A plot of the integrated absorbance as a function of time is shown in Figure 11b. Under dry conditions, absorptions in this region correspond to absorptions bands of oxide-coordinated nitrate on the surface. At higher relative humidity, the spectrum changes with the appearance of two broad absorptions near 1390 and 1300 cm^{-1} indicative water-solvated nitrate on the particle surface.

The rate of HNO_3 uptake on α-Al_2O_3 particles has been investigated in the presence of adsorbed water which was varied by doing experiments at different relative humidity. The same experimental procedure described above was followed except that the oxide particles in the infrared cell were exposed to mixtures of HNO_3 and H_2O vapor. The kinetic data collected under dry and wet conditions were analyzed according to the procedure described in Goodman et al.[31] The integrated absorbances (or peak heights) were calibrated to surface coverage (molecules cm^{-2}) using volumetric methods. Along with the calibration, the linear portion of the integrated absorbance versus time curves is used to calculate the rate of adsorption (dN_a/dt). The gas flux is calculated from the kinetic theory of gases. And the uptake coefficient, as defined in eq 2, is just the ratio of the rate of adsorption to the gas flux. For the experiments with water vapor present, it was necessary to increase the HNO_3 concentration as some of the gas-phase HNO_3 was lost in the water layer on the reaction vessel walls. The increased uptake on the walls was determined in separate experiments. Therefore, the measured uptake is a lower limit as the gas flux to the surface is overestimated in the analysis of γ.

The increase in the uptake coefficient on the wetted surface as a function of relative humidity is shown in Figure 11c. The open circles represent the enhancement in the reactive uptake coefficient, $\gamma_{wet}/\gamma_{dry}$, of HNO_3 on α-Al_2O_3 particles as a function of relative humidity. The data are collected only up to 17% RH because the rate of adsorption became too fast to measure. The solid line represents the 3-parameter BET isotherm fit for water adsorption on α-Al_2O_3, in which the parameter V_m, the volume of adsorbed water on the oxide particles corresponding to a coverage of one monolayer, was replaced by γ_m, the uptake coefficient measured at a water coverage of one monolayer, as suggested in a recent paper by Davis and Cox for nitric acid uptake on NaCl.[36] This equation can be written as

$$\gamma_{wet} = \left(\frac{\gamma_{wet,m} c\left(\frac{P}{P_o}\right)}{1-\left(\frac{P}{P_o}\right)}\right)\left(\frac{1-(n+1)\left(\frac{P}{P_o}\right)^n + n\left(\frac{P}{P_o}\right)^{n+1}}{1+(c-1)\left(\frac{P}{P_o}\right) - c\left(\frac{P}{P_o}\right)^{n+1}}\right) \quad (12)$$

where

$$c = \exp-\left[\frac{\Delta H_1^{\,o} - \Delta H_2^{\,o}}{RT}\right]$$

ΔH_1^0 is the standard enthalpy of adsorption of the first layer, ΔH_2^0 is the standard enthalpy of adsorption on subsequent layers and is taken as the standard enthalpy of condensation, R is the gas constant, T is the temperature in K, P is the pressure, P_o is the saturation pressure, and n is the limiting number of water layers at high pressures.

The BET parameters for the isotherm curve for water uptake on α-Al_2O_3 particles become $\gamma_{wet,m} = 1.82 \times 10^{-6}$ at 16% RH with $c = 25.2$ and $n = 8$. In the case of CaO, the BET isotherm curve for water uptake on nitrate-covered CaO particles was used to model the γ dependence. Similar to $CaCO_3$, the CaO water uptake capacity increased after reaction with nitric acid. The parameters for CaO are $\gamma_{wet,m} = 9.90 \times 10^{-6}$ at 13% RH with $c = 39.7$ and $n = 4.1$. The ratio of $\gamma_{wet}/\gamma_{dry}$ as a function of relative humidity and the calculated $\gamma_{wet}/\gamma_{dry}$ from the water isotherm curve shows that the HNO_3 uptake rate on oxide particles is enhanced in the presence water vapor and that this enhancement can be understood in terms of the increased adsorbed water layers on the oxide particles.

Inclusion of Heterogeneous Uptake of HNO_3 in an Atmospheric Chemistry Box-Model. To study the interactions between aerosols and the photochemical oxidant cycle, it is necessary to treat particles and the gas-phase chemistry processes in a coupled fashion. Carmichael and co-workers have developed a combined aerosol/gas-phase chemistry model for this purpose, in which the detailed multicomponent aerosol dynamics and heterogeneous chemistry on the aerosol surface are explicitly included in the model formulation.[14,52] It is their model and modeling analysis that are described here. In the model, aerosol interactions with the photochemical oxidant cycle arise through the sorption of trace species and the gas-to-particle conversions of nitrogen and sulfur species during the aerosol growth and surface heterogeneous reaction processes. Gas-to-particle conversion, coagulation and deposition are important dynamic processes that are also treated. Box-model simulations were performed using the gas-phase mechanism that is in the STEM-II model.[53] The gas-phase chemical mechanism is based on that of Lurmann et al.[54] but has been modified to include low NO_x conditions and an explicit treatment of isoprene. It consists of 83 chemical species and 185 gas-phase reactions. The effect of aerosol on the actinic flux is also included in the analysis through the use of a 2-stream radiation model.[55,56]

The interactions between the gas and aerosol phases were modeled using the kinetics approach. This approach has been taken by several investigators for the purpose of modeling the interaction between the gas-phase species and the dust/aerosol particles.[13,14,57,58] For the calculation of dC_i/dt, where C_i is the adsorbed species concentration, the following equations are used[14,57−59]

$$\frac{\partial C_i}{\partial t} = \int_{r_2}^{r_1} 4\pi r^2 F(r) \frac{dn}{dr} dr \quad (13)$$

$$F(r) = \frac{D_j(C_j - C_j^e)/r}{1 + f(K_n,\gamma)K_n} \quad (14)$$

$$f(K_n,\gamma) = \frac{1.333 + 0.71K_n^{-1}}{1 + K_n^{-1}} + \frac{4(1-\gamma)}{3\gamma} \quad (15)$$

where C_j is the gas-phase concentration of the absorbing species, C_j^e is the equilibrium gas-phase concentration of species j that would be in equilibrium with the surface adsorbed species (this term can be related to surface coverage and surface saturation effects), D_j is the gas-phase diffusion coefficient in $cm^2\ s^{-1}$, K_n is the dimensionless Knudsen number ($=\lambda/r$), λ is the effective free path of a gas molecule in air, r is the particle radius, $F(r)$ is the flux of the trace species to the surface of the aerosol particle with radius r in molecules $cm^{-2}\ s^{-1}$, dn/dr is the number-size distribution of aerosol particles, and γ is the accommodation or uptake coefficient (sometimes denoted as α). Though it is formally possible to separate the uptake coefficient into an adsorption component and a reaction component, no such distinction is made here and γ represents the net loss to the sample as it does in the laboratory measurements.

These equations show that the molecular flux onto free molecular regime particles ($K_n > 10$) is proportional to the second moment of the size distribution, whereas the molecular flux onto continuum regime particles ($K_n < 0.1$) is proportional to the first moment. Because the aerosol size-distributions used in this modeling study range from free molecular to continuum

TABLE 3: Summary of the Initial Physical and Chemical Conditions Used in the Box-Model Simulation

initial conditions	
species	concentration (ppb)
NO	1.5
NO_2	0.5
HNO_3	0.0005
NH_3	1.0
SO_2	8.0
H_2SO_4	0.8
O_3	50.0
C_2H_6	2.843
C_3H_8	1.379
ALKANE[a]	1.233
C_2H_4	3.461
ALKENE[b]	0.692
AROMATIC	6.290
C_2H_2	0.895
H_2O_2	2.0
ISOPRENE	5.0
Dimethyl sulfide	0.005
H_2S	0.001
CO	150.0
meteorological and other factors:	
T (K)	300 K
R. H.	80%
dry deposition included	
γ_{HNO_3}	$\{10^{-4}, 10^{-3}, 10^{-2}, 10^{-1}\}$
mass loading	160 to 400 $\mu g/m^3$

[a] ALKANE denotes higher alkane than propane. [b] ALKENE denotes higher alkene than ethene.

regimes, the actual molecular flux onto aerosol particles falls between these two limits.

To assess the importance of the heterogeneous reaction of HNO_3 on mineral oxides and dust, a box-model analysis was performed for various chemical regimes. Conditions representative of Cheju, Korea were considered. Cheju is an island located in the East China Sea, which is impacted by anthropogenic pollution and mineral aerosol during the frequent continental outflow events in the spring. The values used for emission rates and dry deposition rates were taken from Sander and Crutzen.[57] Other conditions used in the simulation are given in Table 3.

Heterogeneous uptake rate constants for the specified size distribution were calculated using a log-normal distribution was utilized for the aerosol number-size distribution.[14,60] The log-normal number-size distribution is expressed in the following manner

$$\frac{dN(r)}{d(\log r)} = \sum_{i=1}^{3} \frac{n_i}{\log\sigma_i\sqrt{2\pi}} \exp\left\{\frac{-(\log r/R_i)^2}{2(\log \sigma_i)^2}\right\} \qquad (16)$$

where r is the particle radius in μm, $N(r)$ is the cumulative particle number distribution in cm^{-3} for particles larger than r, R is the mean particle radius in μm, n is the integral of the normal function, and log σ is a measure of particle polydispersity. The parameters for the Cheju simulation were taken from Zhang et al. (1994) : $n = 7.98$, $r = 0.88$ μm, and $\sigma = 0.23$. For these parameters, the geometric surface area is 0.85 m^2g^{-1}. Although the laboratory data show that there are some differences in the uptake coefficients determined for different oxides and dust samples, the current model only takes into account a size distribution and does not take into account chemical heterogeneity of the mineral dust particles. A maximum surface coverage for nitric acid is taken as 5×10^{14} molecules cm^{-2}.

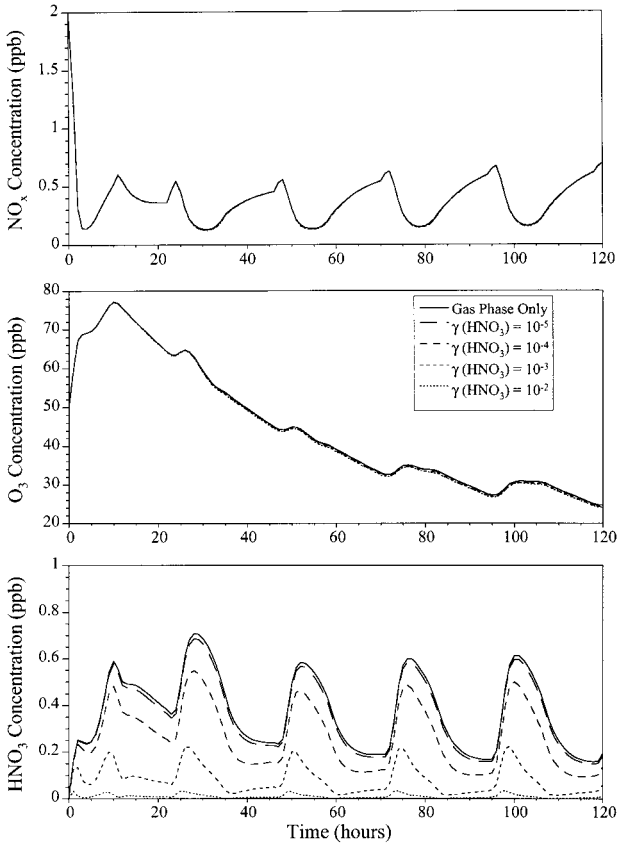

Figure 12. Effect of heterogeneous uptake of HNO_3 on O_3, NO_x, and HNO_3 concentrations. Simulation details are given in Table 3.

After this coverage, the heterogeneous reactivity for that particle is zero, i.e., γ is set equal to zero.

The impact of the heterogeneous reaction of HNO_3 on mineral surfaces was simulated and the results are shown in Figure 12. The box-model calculations show a comparison between a simulation done with gas-phase only processes to simulations where heterogeneous uptake of HNO_3 is also included. Box-model simulations showed that γ_{HNO3} must be greater than 10^{-5} for these processes to be important under the conditions studied. On the basis of this, the Knudsen cell results indicate that the nitric acid reaction is clearly significant. As expected, the heterogeneous loss of HNO_3 results in a large decrease in predicted HNO_3 concentrations and HNO_3 to NO_x ratios. However, the effect of a pure heterogeneous loss of HNO_3 on O_3 and NO_x levels is small. For $\gamma_{HNO_3} = 10^{-3}$, no effect is found in the calculated mixing ratios of O_3 or NO_x whereas that of HNO_3 is reduced by 30%. The conclusions based on the models are for NO_x limited regimes as most regions are NO_x limited.

The Knudsen cell results should be viewed as a lower limit estimate for a variety of reasons. One important consideration is that these experimental results represent very dry conditions. As discussed here, γ_{HNO_3} is greatly enhanced by surface adsorbed water. Under conditions that more closely simulate the atmosphere, i.e., 20−90% RH, it is is shown next that γ_{HNO_3} is significantly increased. In addition, at high RH, the nitrate coating formed on mineral dust from heterogeneous HNO_3 participates in the hygroscopic deliquescence and efflorescence cycles. These cycles are influenced by the presence of mineral dust.[61−64] A second important consideration is that the maximum particle surface coverage allowed in the simulation was 5×10^{14} molecules cm^{-2}. After this coverage is reached, the heterogeneous reactivity for that particle is zero. For mineral dust particles containing $CaCO_3$, CaO, and MgO, this coverage

is probably too small as these particles have reactivity that extends into the bulk of the particle under conditions of RH relevant to the troposphere. Other studies done at lower pressures that only take into account the geometric area of the sample holder have suggested that the initial uptake is higher than those reported here.[65,66] A study on a single-crystal surface of α-Al_2O_3 reported[65] an initial uptake of 1×10^{-3} was shown to be an experimental artifact. [66]

4. Heterogeneous Conversion of NO_2 to HONO on Wetted-SiO_2 and Soot Particles

Hydroxyl radical is the most important trace species in atmospheric oxidation mechanisms.[67,68] Although it is clear that O_3 photolysis is the main source of OH radicals in the stratosphere, mechanisms for OH radical formation in the troposphere are still being debated. One source of hydroxyl radical is from the photodissociation of nitrous acid (HONO), as HONO undergoes photolysis at wavelengths between 330 and 380 nm[69]

$$\mathrm{HONO} + h\upsilon \rightarrow \mathrm{OH} + \mathrm{NO} \qquad (17)$$

Although HONO concentrations up to 14 ppb have been observed in polluted urban environments, HONO formation is not well understood.[70,71] Lee and Schwartz[71] have shown that reactions 18 and 19 are too slow in the gas and aqueous phases to be relevant under atmospheric conditions

$$\mathrm{NO_2} + \mathrm{NO} + \mathrm{H_2O} \rightarrow 2\mathrm{HONO} \qquad (18)$$

$$2\mathrm{NO_2} + \mathrm{H_2O} \rightarrow \mathrm{HONO} + \mathrm{HNO_3} \qquad (19)$$

Evidence suggests, however, that these reactions may occur at a faster rateby a heterogeneous or surface-catalyzed mechanism.[73−86] In fact, surface reactions may be responsible for as much as 95% of all the HONO found in the troposphere.[75,77,78] A recent review article discusses the evidence presented for heterogeneous reaction of NO_2 to produce gas-phase HONO in humid environments.[84] The reaction proceeds over a wide variety of surfaces including those of glass, sodium halides, metals, and metal oxides.

Several laboratory studies have reported that heterogeneous HONO formation via reaction 20 is first order in both NO_2 and H_2O[75−78,84]

$$\mathrm{d[HONO]}/\mathrm{d}t = k\,[\mathrm{NO_2}][\mathrm{H_2O}] \qquad (20)$$

with the rate-limiting step being adsorption of NO_2. Using environmental chambers containing NO_2 and H_2O, Sakamaki et al.[74] and Pitts et al.[75] proposed that reaction 19 provides the best model for the heterogeneous formation of HONO although no HNO_3 was directly detected. Therefore, without full characterization of all of the reactants and products in reaction 19, the reaction has been considered somewhat speculative.[76] The lack of any observable HNO_3 in the gas phase has been explained by the suggestion that it sticks to the walls of the environmental chamber. This suggestion is supported in some recent experiments in which HNO_3 was detected via ex-situ measurements.[77,85]

Heterogeneous reactions on carbonaceous aerosol may also provide a reactive surface for formation of HONO in the atmosphere. The heterogeneous reaction of nitrogen oxides, in particular NO_2, on carbonaceous aerosol has been studied by several groups using a variety of experimental techniques.[3,86−99] It has been shown that NO_2 can react with soot particles to produce HONO. It has been proposed that this reaction on soot may account for the high concentration of HONO observed during night time when the homogeneous reaction is insignificant. The reaction involves adsorbed hydrogen on the soot surface with gas-phase NO_2 according to reaction 21.

$$\mathrm{NO_2\,(g)} + \mathrm{H\,(a)} \rightarrow \mathrm{HONO\,(g)} \qquad (21)$$

However, there is a range of values reported for the heterogeneous uptake coefficient of NO_2 on soot, from 0.095 to 10^{-6}, a range that spans nearly 5 orders of magnitude. This discrepancy in the values of the uptake coefficient arises in part because soot samples are often from different sources. Commercial soot differs from freshly prepared soot, and even the later can be prepared in different ways using different hydrocarbons. This means that from study to study soot particles can have different chemical composition, different sizes, different BET surface areas, and, therefore, different reactivities. Experimental conditions such as temperature, relative humidity, and pressure of NO_2 are also varied from one study to another. Another source of discrepancy is that the accessible surface area for reaction must be accurately accounted for when calculating uptake coefficients. NO_2 is thought to diffuse to the pores of soot samples and access underlying layers of particles in bulk samples.[85,94] However, in some of the above studies,[86,87,91] only uptake on the first layer of soot was considered, and thus the exposed geometric area of soot was used in calculating γ. This may explain the very high γ-values reported in some studies compared to others. In addition, in all of the studies discussed above, surface areas were not measured for the soot samples under investigation. This is usually done using the BET method and N_2 as the adsorbent molecules. Instead, values were taken from the literature, which may or may not accurately represent the true values because of differences in sample preparation. The fractal nature of soot also makes the characterization of the available surface area difficult. As noted by Longfellow et al.,[86] in order to apply laboratory measurements of the heterogeneous uptake measurements to the atmosphere, the surface area of the soot must be considered. One other difference in the literature values is that the initial uptake coefficients are reported in some cases, whereas a steady-state or an average value is reported in others. This means that the reactivity of a surface covered with adsorbed molecules is compared to the reactivity of the unreacted surface. Because of site-blocking, adsorbate−adsorbate interactions, and electronic effects, uptake coefficients are typically coverage dependent and usually decrease as a function of coverage.[94]

To have a greater understanding of heterogeneous formation of HONO in the global troposphere, FT-IR, Knudsen cell and aerosol chamber experiments have been conducted for the NO_2 reaction on wetted-silica particles, to investigate reaction 19, and soot, to investigate reaction 21. These experiments are described in the following sections.

Spectroscopic Measurements of the Heterogeneous Reaction of NO_2 on Soot and Wetted SiO_2 Particles. In contrast to other oxides investigated, including α-Al_2O_3, α-Fe_2O_3, and TiO_2,[101,102] there is little change in the spectrum of SiO_2 particles upon exposure of NO_2 to dehydrated samples. However, when NO_2 is added to the infrared cell containing hydrated SiO_2 particles with a surface coverage of approximately 0.08 monolayers of adsorbed water, absorption bands appear in the silica spectrum at 1677, 1399, and 1315 cm^{-1} (Figure 13a). As discussed below, these bands can be assigned to the vibrational modes of adsorbed HNO_3. The assignment of the bands to adsorbed HNO_3 is confirmed by the spectrum of an authentic

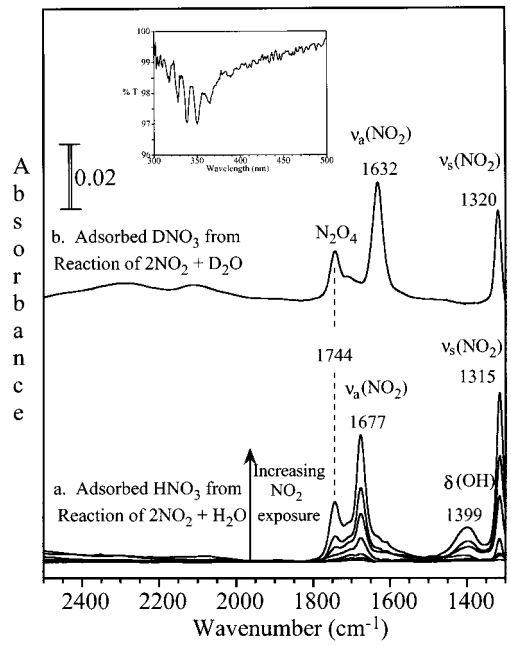

Figure 13. (a) FT-IR spectra of hydrated SiO_2 recorded as a function of NO_2 pressure (0.058, 0.117, 0.237, 0.625, 1.318, 2.011, and 3.417 Torr). (b) FT-IR spectrum recorded following reaction of NO_2 (1.318 Torr) on SiO_2 in which adsorbed H_2O had been exchanged with D_2O. The UV−Vis transmission spectrum of HONO produced from reaction of NO_2 with in the presence of 16 mg of hydrated SiO_2 is shown in the inset.

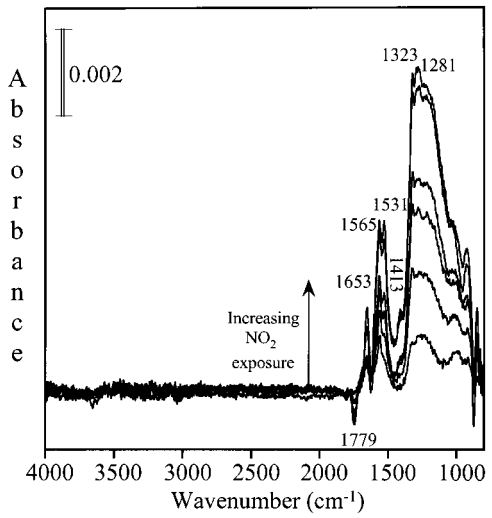

Figure 14. FT-IR spectra of the hexane soot surface recorded as a function of NO_2 exposure. The assignment of these peaks are as follows; 1281 cm^{-1} −R−ONO, 1323 cm^{-1} −R−NO_2, 1413 cm^{-1} −CO_3^{2-}, 1531 cm^{-1} −R−NO_2, 1565 cm^{-1} −R−N−NO_2, 1653 cm^{-1} −R−ONO, and 1777 cm^{-1} -lactone and alkyl carbonyl groups.

sample of HNO_3 adsorbed on SiO_2. The three bands in the spectrum can be assigned to $\nu_a(NO_2)$ − 1677 cm^{-1}, δ(OH) − 1399 cm^{-1}, and $\nu_s(NO_2)$ − 1315 cm^{-1} modes of adsorbed HNO_3. These bands are shifted by 10−68 cm^{-1} from the gas-phase HNO_3 frequencies,[103] but compare well to the infrared spectrum of HNO_3 in highly concentrated aqueous solution which has absorptions at 1670 cm^{-1} and 1300 cm^{-1} that are assigned to the ν_a (NO_2) and ν_s (NO_2) modes, respectively.[104] The OH stretching region (not shown) is complicated and showed an intense broad absorption band extending from 3700 to as low as 2700 cm^{-1}. This broadband is most likely due to a hydrogen bonding interaction between HNO_3 and H_2O. Experiments done with adsorbed D_2O confirm these assignments (Figure 13b).[105,106]

According to reaction 19, the production of gas-phase HONO is also expected from the heterogeneous reaction of NO_2 on hydrated SiO_2 particles. The gas-phase UV−Vis spectrum obtained by reacting NO_2 on hydrated SiO_2 is shown in the inset of Figure 13.

Previous to our study,[105] a full in-situ characterization of the products of the reaction, $2NO_2$ (g) + H_2O(a) → HONO(g) + HNO_3 (a), has not been made. This is the first direct evidence for the surface reaction between gas-phase NO_2 and adsorbed H_2O to yield both adsorbed and gas-phase products. Barney and Finlayson-Pitts have confirmed these results in an analogous study of NO_2 adsorption on porous silica glass.[104]

The NO_2/soot reaction was also examined by FT-IR spectroscopy.[108] The FT-IR data show that adsorbed products remain on the surface for the NO_2 soot reaction as well. Figure 14 shows the FT-IR spectra of hexane soot (1 mg) as a function of NO_2 exposure. The infrared spectra recorded as a function of increasing exposure of NO_2 by increasing the pressure from 5 to 100 mTorr are shown in Figure 14. These spectra were recorded in the presence of gas-phase NO_2, and the unreacted soot surface is taken as the reference background spectrum. All spectra are shown in both Figures 13 and 14 are recorded after the surface becomes equilibrated with the gas phase, as is evident by the fact that the pressure remains constant and the spectra are no longer changing. The spectra showing only surface-bound products show bands at 1281, 1323, 1531, 1565, and 1653 cm^{-1} that increase as the coverage of NO_2 is increased. These bands are associated with the following functional groups; 1281 cm^{-1} −R−ONO, 1323 cm^{-1} −R−NO_2, 1413 cm^{-1} −CO_3^{2-}, 1531 cm^{-1} −R−NO_2, 1565 cm^{-1} −R−N−NO_2, and 1653 cm^{-1} −R−ONO and are in agreement with other FT-IR studies.[91,96]

There is a decrease in the intensity of the band at 1777 cm^{-1} suggesting the loss of C═O group from the carbonyl surface, presumably due to the formation of gas-phase CO_2 or CO as has been observed in other studies done at high pressures of NO_2.[93] Upon evacuation of the gas phase, the infrared spectrum of the surface remains nearly identical with only a small decrease (<5%) in intensity of the bands between 1400 and 1675 cm^{-1}.

Knudsen Cell Measurements for the Heterogeneous Uptake of NO_2 on Wetted SiO_2 and Soot. Knudsen cell measurements provided additional insight into the reaction of NO_2 and H_2O. In these experiments, the SiO_2 particles were covered with a lid, while a steady-state flow of NO_2 was established. Once steady-state flow was reached, the lid was then opened to expose the particles to the gas. These measurements were carried out on SiO_2 particles that contained different amounts of adsorbed water. SiO_2 particles evacuated overnight to a pressure of $< 1 \times 10^{-6}$ Torr (labeled dehydrated SiO_2) showed no measurable loss of NO_2 from the gas phase, as seen in Figure 15. SiO_2 particles evacuated for shorter periods of time did show a measurable amount of NO_2 uptake. Data are presented in Figure 15 for SiO_2 particles that were exposed to 10 Torr of water at 298 K followed by evacuation for twenty minutes. There is a decrease in NO_2 flow rate and reaction on hydrated SiO_2 particles when the lid was open. There is an initial spike in the NO_2 flow rate, but then the flow rate approaches the steady-state value. The lid was closed again for 300 s and subsequently the oxide particles were exposed. The second time the lid was open there was less of a decrease in the NO_2 signal and the reaction, as indicated by the NO_2 signal ends quickly.

The H_2O flow rate for the two SiO_2 samples, dehydrated and hydrated, is also shown in Figure 15. The H_2O signal increases

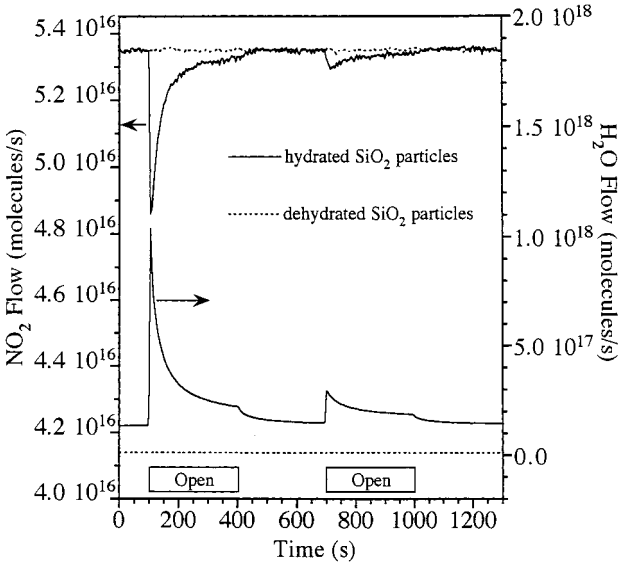

Figure 15. Flow cell reactor mass spectral data for reaction of NO_2 on SiO_2. The flow rate in molecules per second is shown for two gas-phase molecules, NO_2 (scale for NO_2 flow is shown on the *y*-axis on the left) and H_2O (scale for H_2O flow is shown on the *y*-axis on the right) during reaction on dehydrated and hydrated SiO_2. At time t = 100 s, the sample holder is opened and there is a drop in the NO_2 flow rate as NO_2 reacts on the surface of hydrated SiO_2 particles (i.e., particles exposed to 10 Torr H_2O overnight and evacuated for 20 min) but not dehydrated SiO_2 particles (i.e. particles evacuated overnight). The sample holder is then closed and the NO_2 signal returns to its baseline value. The process of exposing the surface to NO_2 was repeated once again. The plot also shows that there is a significant amount of water outgassing from the hydrated but not the dehydrated sample.

when the lid is open indicating that water is outgassing from the SiO_2 sample. There are several points that can be made concerning the H_2O desorption from the SiO_2 samples. First, the amount of water coming from the SiO_2 sample labeled "dehydrated" is a factor of 100 times less than the SiO_2 samples labeled "hydrated". Second, the amount of adsorbed water on the hydrated sample significantly decreases as the water outgassed from the sample. Third, there is a concomitant decrease in the NO_2 uptake with the decrease in the amount of adsorbed H_2O. It was difficult to determine an uptake coefficient for this reaction as it is not clear how water is distributed through the sample in these experiments, thus, the coverage of adsorbed water is unknown.

As described here, it is much easier to quantify the NO_2/soot reaction. In these experiments, soot is directly deposited onto the Knudsen cell sample holder that is 11.95 cm^2 in area. Initial uptake coefficient for the reaction of NO_2 with hexane soot was measured as a function of sample mass (and thus sample thickness). Representative Knudsen cell data are shown in Figure 16. The QMS intensity of NO_2 (m/e = 46) was monitored during the experiment (Figure 16a). When the sample lid is open and the soot particles are exposed to the reactive gas, there is a decrease in the QMS intensity. The QMS intensity of NO_2 is then converted to the observed uptake coefficient via eq 8 as shown in Figure 16b. The initial observed uptake coefficient, $\gamma_{o,obs}$ is taken as the maximum value for γ and found to be 0.018 from the data shown in Figure 16b. It can be seen from the data plotted in Figure 16b that over time the value of the uptake coefficient decreases as the reaction proceeds. This decrease occurs because the surface becomes less reactive with continued reaction of NO_2 and is interpreted as a coverage dependent uptake coefficient.

Nitrous acid is detected as a product in the NO_2 reaction with soot. The QMS intensity for the parent ions of NO_2 and HONO, m/e = 46 and 47, respectively, were calibrated and converted to molecular flow through the Knudsen cell. These data are shown in Figure 16c. The flow of NO_2 has been offset and inverted to show the amount of NO_2 that reacts per second. Because the m/e = 47 signal from the mass spectrometer

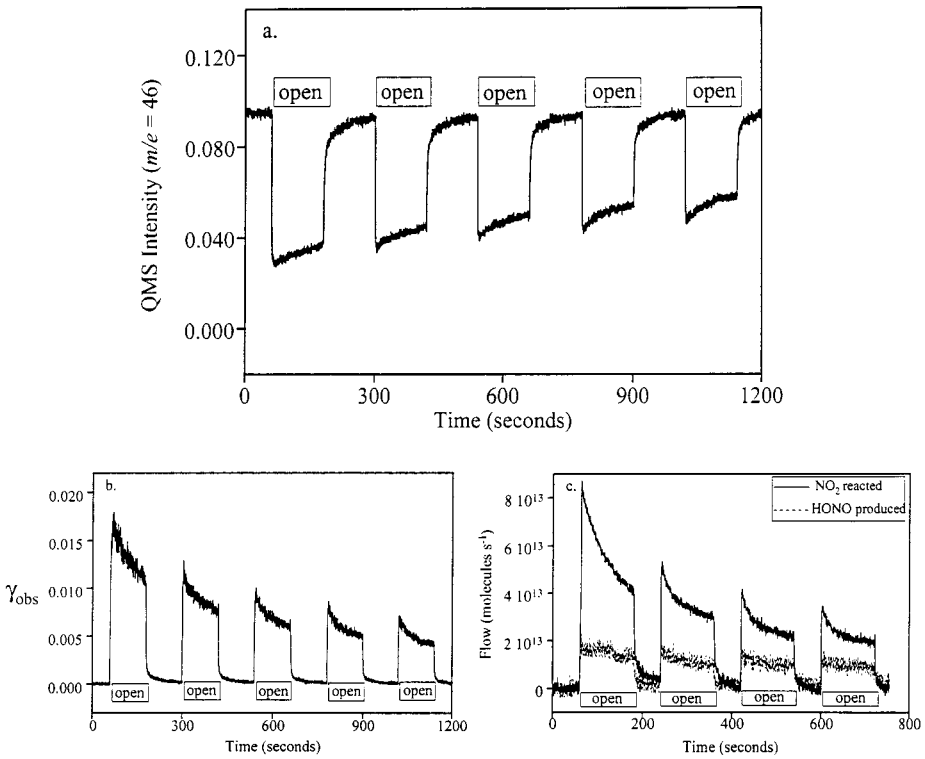

Figure 16. (a) Knudsen cell data for the heterogeneous reaction of NO_2 on soot (15.1 mg sample). The QMS intensity for m/e = 46 is shown. (b) Observed uptake coefficient calculated via eq 8 from the data shown in a. Calibrated flow of NO_2 reacted and HONO produced (7.7 mg sample).

contains two contributions, the parent ions of HONO and the natural abundance ^{15}N labeled NO_2, calibration of the $m/e = 47$ signal for HONO production was done according to the procedure outlined previously.[105] From the calibrated data presented in Figure 16c, the amount of HONO produced per NO_2 reacted is determined to be $36 \pm 5\%$. The remaining NO_2 taken to the surface may correspond to the formation of surface-bound products (vide infra) and other gas products such as NO. The percentage of HONO produced in this study is lower than that reported in another Knudsen cell study.[87] This may be a result of using different hydrocarbon as a soot generator and collecting soot at different heights from the flame base.[85,93]

From the calibrated data it is also possible to determine the absolute number of NO_2 molecules reacted per unit surface area (or unit mass of soot). For small masses of soot (< 1 mg), complete saturation of the surface can be obtained by continuing the reaction until no further uptake of NO_2 is observed. This means that over time the uptake coefficient goes to zero. The data in Figure 16c can be used to determine the total amount of NO_2 reacted per unit surface area. For thin or low mass samples, complete saturation occurs over the time period of the experiment. For thicker samples with larger mass, the data are fit to a double exponential form and the fit is then extrapolated to the limit of no further uptake of NO_2 corresponding to a saturated surface. From all of the data, it is determined that the total amount of NO_2 that can react at a pressure near 8 μTorr is determined to be $1.4 \pm 0.5 \times 10^{13}$ molecules cm^{-2} or $1.1 \pm 0.4 \times 10^{16}$ molecules mg^{-1} of soot. This value is used as the saturation coverage for NO_2 on soot at 295 K and a pressure of 8 μTorr and is lower than the value obtained for studies of NO_2 on soot measured at higher pressures.[95,98]

The value of the observed initial uptake coefficient is found to depend on the number of layers of soot present. The observed initial uptake coefficient measured as a function of the sample mass is plotted in Figure 17a. Because the sample holder is a fixed area, 11.95 cm^2, increasing the sample mass increases the number of layers of soot. The line through the data is determined from the KML gas-diffusion model discussed in the Experimental Methods and Data Analysis Section. The parameters listed in the figure caption were used as input data in the diffusion model for the reaction of NO_2 with hexane soot. There are two parameters that are adjusted in order to obtain a good fit, the true initial uptake coefficient, $\gamma_{o,t}$, that takes into account the accessible surface area of the underlying layers and the tortuosity, τ, which is related to the diffusion of the molecules through the sample.

There are two regions in the plot shown in Figure 17a. The region that extends from 0 to approximately 8 mg shows that the observed initial uptake coefficient has a nearly linear dependence on sample mass. The portion of the plot above 8 mg shows the observed initial uptake coefficient is in the plateau region and shows much less of a dependence on the sample mass. The region above 8 mg shows that the probe depth of the gas-phase molecules measured during this initial time is constant and equivalent to the probe depth reached for a sample of mass of 8 mg. In other words, on the time-scale of the measurement of the initial uptake coefficient, NO_2 molecules are diffusing into only a portion of the soot sample estimated to be on the order of one thousand layers. For thin samples, the time-scale for the observed uptake coefficient to reach its maximum value is on the order of the residence time (approximately 2 s). For a sample mass of 7.7 mg, this time-scale is slightly longer, on the order of 3.5 s for the molecules to diffuse through all of the underlying layers.

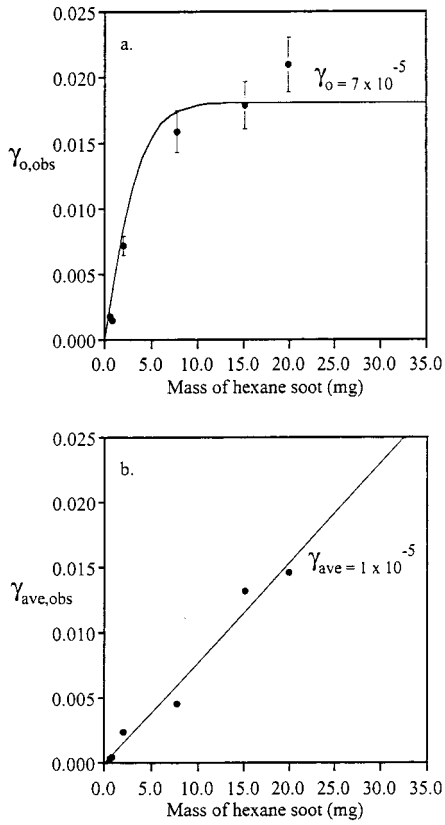

Figure 17. (a) The mass dependence (thickness dependence) of the initial uptake coefficient for the reaction of NO_2 with hexane soot. Filled circles (●) represent experimental data, the solid line (−) is the result of a KML fit to the data. The experimental and fitting parameters used in the model are as follows; $\rho_b = 0.1$ g cm^{-3}, $\rho_t = 2.0$ g cm^{-3}, $d = 3.9 \times 10^{-6}$ cm, $S_{BET} = 760$ cm^2 mg^{-1}, $\tau = 1$, and $\gamma_{o,t} = 7 \times 10^{-5}$. (b) The mass dependence of the average uptake coefficient, averaged over 120 s. Filled circles (●) represent experimental data and the solid line (−) represent a linear least-squares fit to the data of the form $y = mx$. The slope of the fit is 7.7×10^{-4} mg^{-1} with an R factor of 0.986.

Also shown in Figure 17 is an average observed uptake coefficients calculated over a 120 s time period. The data plotted in Figure 17b show $\gamma_{ave,obs}$ as a function of mass of *n*-hexane soot. It is seen that $\gamma_{ave,obs}$ is a linear function of sample mass over the entire range. The average uptake coefficient can be corrected for the accessible BET area using a linear least-squares fit of the line through the data points. This correction is then obtained from eq 8. The value calculated for $\gamma_{ave,obs}$ is 1×10^{-5}. This is a factor of 6 times lower than the initial value of the uptake coefficient. Although the application of the diffusion model in Figure 17a predicts a nearly linear mass regime to be in the range from 0 to 8 mg for the initial uptake coefficient, the dependence of the average uptake coefficient on the mass is still linear up to 19 mg.

Heterogeneous Conversion of NO_2 to HONO in the Troposphere and Other Potentially Important Heterogeneous Reactions Involved in HONO Formation. The heterogeneous conversion of NO_2 to HONO can occur on wetted-SiO_2 and soot aerosol. Two questions that can be asked, do these reactions contribute to the formation of HONO in the global troposphere and do they contribute to NO_2 loss. The reaction probability measured for the heterogeneous reaction of NO_2 and H_2O, according to reaction 19 has been investigated and discussed. According to Saliba et al.,[109] this reaction could account for 0.9 ppb of HONO over an 8-h period. For the NO_2 reaction with soot, reaction 21, it has been estimated that it could generate over 10 times more HONO than that due to the

heterogeneous reaction of NO_2 and H_2O.[94] However, surface deactivation was not taken into account in this calculation. The laboratory studies presented here indicate that the soot surface does in fact deactivate with time and the production of HONO from this reaction will thus be significantly less than previously calculated. This conclusion is in agreement with a very recent study by Saathoff et al.[99] Further analysis of this reaction would require additional experimentation under more atmospherically relevant conditions that span the temperature and relative humidity range of the troposphere. The effect of heterogeneous reactions on NO_2 levels in the atmosphere appears to be negligible as indicated by a recent laboratory and box-model analysis by Underwood et al.[102]

In 1997, Fairbrother, Sullivan, and Johnston proposed several potential surface-catalyzed reactions for HONO formation.[110] Although these reactions are not kinetically favorable, they were determined to be thermodynamically favorable and thus potentially could be important if surface catalyzed. Many of these reactions involve nitric acid. These reactions include

$$HNO_3 + H_2CO \rightarrow 2HONO + CO_2 + H_2O \quad (22)$$

$$HNO_3 + CO \rightarrow HONO + H_2O + O_2 \quad (23)$$

$$HNO_3 + H_2O_2 \rightarrow HONO + CO_2 \quad (24)$$

$$HNO_3 + NO \rightarrow HONO + NO_2 \quad (25)$$

Saliba et al. have discussed the potential importance of reaction 25 on porous silica surfaces, and suggest it may contribute as much as reaction 19 to HONO production in polluted urban atmospheres.[109] The importance of these reactions on other surfaces will ultimately depend on the reactivity of adsorbed nitric acid.

5. Conclusions and Future Outlook

The laboratory and modeling studies presented here suggests that there is compelling evidence that heterogeneous chemistry is important and plays a role in the chemical balance of the troposphere. Water plays an important role as a solvent that can facilitate the dissociation of ionic species and as a reactant in HONO formation. Heterogeneous reactions should be included in atmospheric chemistry models if the models are to adequately describe the details of all molecular level processes that occur in the atmosphere. There is still much to be explored in laboratory studies of heterogeneous reactions on solid particles present in the atmosphere. Some of the questions that remain include the following:

- What additional reactions take place on aerosol surfaces, and what are the reaction products (in the gas and or aerosol phase)? How do they influence gas-phase compositions (e.g., do they alter $NO_2/HO_x/O_3$ distributions)?
- How do these chemical processes impact aerosol composition and properties (e.g., can they alter radiative properties)?
- Under what conditions are such reactions expected to be important (at night, in urban environments, upper troposphere, etc.)?
- What are the best experimental methods for measuring heterogeneous reaction kinetics under the relevant conditions appropriate troposphere?

Complementary laboratory studies and atmospheric chemistry modeling as well as field studies will be important in addressing these questions and issues.

Acknowledgment. The research described herein could not have been done without the expertise and efforts of many individuals. My collaborator Professor Gregory Carmichael has been an invaluable resource. He and his group provided the modeling analysis to this project. Former students of my research group, Drs. Todd Miller and Angela Goodman, as well as former postdoctoral scientists, Drs. Grant Underwood and Ping Li, were instrumental in developing the experimental apparatus and expertise needed for these studies. Current graduate students Hind Al-Abadleh and Courtney Usher have also contributed to this work and continue with these studies along with Brenda Krueger, Sofia Carlos-Cuellar, Adam Christensen, Jennifer Wade, Hashim Al-Hosney and Dr. Amy Michel. This work would not have been possible without funding from the National Science Foundation (CHE-9988434 and CHE-9614134), Department of Energy Atmospheric Chemistry Program (DE-FG01-98ER62580) and the Camille and Henry Dreyfus Postdoctoral Program in Environmental Science. The support provided by these agencies and foundation is gratefully acknowledged. Seed grants funded through the University of Iowa's Carver Scientific Research Grant Program, The Center for Global and Regional Environmental Research and The Environmental Health Sciences Research Center are also gratefully acknowledged.

References and Notes

(1) Jonas, P.R.; Charlson, R. J.; Rodhe, H. Aerosols. In *Climate Change 1994: Radiative Forcing of Climate Change, and An Evaluation of the IPCC IS92 Emission Scenarios, Intergovernmental Panel on Climate Change*; Houghton, J. T., Meira Filho, L. G., Bruce, J, Lee, H., Callander, B. A, Haites, E., Harris, N., Maskell, K., Eds.; Cambridge University Press: Cambridge, 1995: pp 127−162.

(2) Charlson, R. J.; Schwartz, S. E.; Hales, J. M.; Cess, R. D.; Coakley, J. A.; Hansen, J. E.; Hofmann, D. J. *Science* **1992**, *255*, 423.

(3) Ammann, M.; Kalberer, M.; Jost, D. T.; Tobler, L.; Rossler, E.; Piguet, D.; Gaggeler, H. W.; Baltensperger, U. *Nature* **1998**, *395*, 157.

(4) Gard, E. E.; Kleeman, M. J.; Gross, D. S.; Hughes, L. S.; Allen, J. O.; Morrical, B. D.; Fergenson, D. P.; Dienes, T.; Galli, M. E.; Johnson, R. J.; Cass, G. R.; Prather, K. A. *Science* **1998**, *279*, 1184.

(5) Jacob, D. J. *Atmos. Environ.* **2000**, *34*, 2131.

(6) Ryerson, T. B.; Trainer, M.; Holloway, J. S.; Parrish, D. D.; Huey, L. G.; Sueper, D. T.; Frost, G. J.; Donnelly, S. G.; Schauffler, S.; Atlas, E. L.; Kuster, W. C.; Goldan, P. D.; Hübler, G.; Meagher, J. F.; Fehsenfeld, F. C. *Science* **2001**, *292*, 719.

(7) Ravishankara, A. R. *Science* **1997**, *276*, 1058.

(8) Kolb, C. E.; Worsnop, D. R.; Zahniser, M. S.; Davidovits, P.; Keyser, L. F.; Leu, M.-T.; Molina, M. J.; Hanson, D. R.; Ravishankara, A. R.; Williams, L. R.; Tolbert, M. A. *Prog. Probl. Atmos. Chem.: Adv. Ser. Phys. Chem.* **1995**, *3*, 771.

(9) Molina, M. J.; Molina, L. T.; Kolb, C. E. *Annu. Rev. Phys. Chem.* **1996**, *47*, 327.

(10) Finlayson-Pitts, B. J.; Hemminger, J. C. *J. Phys. Chem. A* **2000**, *104*, 11 463.

(11) Sheehy, D. P. *Ambio* **1992**, *21*, 303.

(12) Dentener, F. J.; P. J. Crutzen, P. J. *J. Geophy. Res.* **1993**, *98*, 7149.

(13) Dentener, F.; Carmichael, G.; Zhang, Y.; Lelifeld, J.; Crutzen.; P. *J. Geophys. Res.* **1996**, *101*, 22, 869.

(14) (a) Zhang, Y.; Sunwoo, Y.; Kotamarthi, V.; Carmichael, G. *J. Appl. Meteorol.* **1994**, *33*, 813. (b) Zhang, Y.; Carmichael, G. R. *J. Appl. Meterol.* **1999**, *38*, 353.

(15) Tabazadeh, A.; Jacobson, M. Z.; Singh, H. B.; Toon, O. B.; Lin, J. S.; Chatfield, R. B.; Thakur, A. N.; Talbot, R. W.; Dibb, J. E. *Geophys. Res. Lett.* **1998**, *25*, 4185.

(16) Bunce, N. *J. Environmental Chemistry*, 2nd ed.; Wuerz Publishing Ltd.: Winnipeg, Canada, 1994.

(17) Golden, D. M.; Spokes, G. N.; Benson, S. W. *Angew Chem., Int. Ed. Engl.* **1973**, *12*, 534.

(18) Caloz, F.; Fenter, F. F.; Tabor, K. D.; Rossi, M. J. *Rev. Sci. Instrum.* **1997**, *68*, 3172.

(19) Golden, D. M.; Manion, J. A.; Reihs, C. M.; Tolbert, M. A. In *The Chemistry of the Atmosphere: Its Impact on Global Change* Calvert, J. G., Ed.; Blackwell Scientific Publications: Oxford, 1994.

(20) Dushman, S. *Scientific Foundations of Vacuum Technique*, 2nd edition; Wiley: New York, 1962.

(21) Aris, R. *The Mathematical Theory of Diffusion; Reaction in Permeable Catalysts*; Clarendon Press: Oxford, 1975, Vol. I.
(22) Keyser, L. F.; Moore, S. B.; Leu, M.-T. *J. Phys. Chem.* **1991**, *95*, 5496.
(23) Underwood, G. M.; Li, P.; Usher, C. R.; Grassian, V. H. *J. Phys. Chem. A* **2000**, *104*, 819.
(24) Fenter, F. F.; Caloz, F.; Rossi, M. J. *J. Phys. Chem.* **1996**, *100*, 1008.
(25) Li, P.; Al-Abadleh, H. A.; Grassian, V. H. *J. Phys. Chem. A* **2002**, in press.
(26) Liu, S. C.; Trainer, M.; Carroll, M. A.; Hubler, G.; Montzka, D. D.; Norton, R. B.; Ridley, B. A.; Walega, J. G.; Atlas, E. L.; Heikes, B. G.; Huebert, B. J.; Warren, W. *J. Geophys. Res.* **1992**, *97*, 14 063.
(27) Chatfield R. B. *Geophys. Res. Lett.* **1994**, *21*, 2705.
(28) Singh, H. B.; Herlth, D.; Kolyer, R.; Salas, L.; Bradshaw, J. D.; Sandholm, S. J.; Davis, D. D.; Crawford, J.; Knodo, Y.; Koike, M.; Talbot, R.; Gregory, G. L.; Sachse, G. W.; Browell, E.; Blake, D. R.; Rowland, F. S.; Newell, R.; Merill, J.; Hiekes, B.; Liu, S. C.; Crutzen, P. J.; Kanakidou, M. *J. Geophys. Res.* **1996**, *101*, 1793.
(29) Phadnis, M.; Carmichael, G. *J. Atmos. Chem*. **2000**, *36*, 285.
(30) Schurath U.; Naumann, K.-H. *Pure & Appl. Chem*. **1998**, *70*, 1353.
(31) Goodman, A. L.; Bernard. E. B.; Grassian, V. H. *J. Phys. Chem. A* **2001**, *105*, 6443.
(32) Beichert, P.; Finlayson-Pitts, B. J. *J. Phys. Chem*. **1996**, *100*, 15 218.
(33) Davies, J. A.; Cox, R. A. *J. Phys. Chem. A* **1998**, *102*, 7631.
(34) Abbatt, J. P. D.; Beyer, K. D.; Fucaloro, A. F.; McMahon, J. R.; Wooldridge, P. J.; Zhong, R.; Molina, M. J. *J. Geophys. Res.* **1992**, *97*, 15, 819.
(35) Molina, M. *The Chemistry of the Atmosphere: Its Impact on Global Change*; Calvert, J. G., Ed.; Blackwell Sci.: Cambridge, 1994; pp 27−38.
(36) Vogt R.; Finlayson-Pitts, B. J. *J. Phys. Chem*. **1994**, *98*, 3747.
(37) Ghosal, S.; Hemminger, J. C. *J. Phys. Chem. A* **1999**, *103*, 4777.
(38) Koch, T. G.; van den Bergh, H.; Rossi, M. J. *Phys. Chem. Chem. Phys.* **1999**, *1*, 2687.
(39) Zangmeister, C. D.; Pemberton, J. E. *J. Phys. Chem. A* **2001**, *105*, 3788.
(40) Donahue, N. M.; Dubey, M. K.; Mohrschladt, R.; Demerjian, K. L.; Anderson, J. G. *J. Geophys. Res.* **1997**, *102*, 6159.
(41) Song, C. H.; Carmichael, G. R. *J. Atmos. Chem.* **2001**, In press.
(42) Song, C. H. 1999, Ph.D. Thesis The University of Iowa, pp 108−146.
(43) Lide, D. R. *Handbook of Chemisty; Physics*; CRC Press: Boca Raton, 1991; pp 4−47.
(44) Peters, J. S.; Ewing, G. E. *J. Phys. Chem. B* **1997**, *101*, 10 880.
(45) Barraclough, P. B.; Hall, P. G. *Surf. Sci*. **1974**, *46*, 393.
(46) Foster, M. C.; Ewing, G. E. *Surf. Sci.* **1999**, *428*, 102.
(47) Foster, M. C.; Ewing, G. E. *J. Chem. Phys.* **2000**, *112*, 6817.
(48) Luna, M.; Rieutord, F.; Melman, N. A.; Dai, Q.; Salmeron, M. *J. Phys. Chem. A* **1998**, *102*, 6793.
(49) Shindo, H.; Ohashi, M.; Tateishi, O.; Seo, A. *J. Chem. Soc.; Faraday Trans.* **1997**, *93*, 1169.
(50) Allen, H. C.; Laux, J. M.; Vog, R.; Finlayson-Pitts B. J.; Hemminger, J. C. *J. Phys. Chem.* **1996**, *100*, 6371.
(51) Allen, H. C.; Mecartney, M. L.; Hemminger, J. C.; *Microscopy; Microanalysis* **1998**, *4*, 23.
(52) Goodman, A. L.; Underwood, Grassian V. H. *J. Geophys. Res.-Atmos.* **2000**, *104*, 29, 053.
(53) Carmichael, G. R.; Peters, L. K.; Saylor, R. D. *Atmos. Environ. A-Gen* **1991**, *25*, 2077.
(54) Lurmann, F. W.; Loyd, A. C.; Atkinson, R. A. *J. Geophys. Res.* **1986**, *91*, 10 905.
(55) Crist K.; Carmichael, G. R.; Hotchkiss, B.; John, K. Effects of Emission Controls; Stratospheric Ozone Loss on Tropospheric Ozone Production. In *Air Pollution Modeling; Its Application XI*, Gryning, Schiermeier, Eds.; Plenum Press: New York, 1996; 155.
(56) Hotchkiss, B. 1996, Ozone, Aerosol; UVB Interactions in the Troposphere in a Combined Radiation/Chemistry Model using ADIFOR. M.S Thesis, Department of Chemical; Biochemical Engineering, The University of Iowa.
(57) Sander, R.; Crutzen, P. J. *J. Geophys. Res.-Atmos.* **1996**, *101*, 9121.
(58) Saylor, R. D. *Atmos. Environ.* **1997**, *31*, 3653.
(59) Fuchs, N. A.; Sutugin, A. G. *Highly Dispersed Aerosols*; Ann Arbor Science: Ann Arbor, MI, 1970.
(60) Jaenicke, R.; Hanusch, T. *Aerosol Sci. Tech*. **1993**, *18*, 309. Jaenicke, R.; Hanusch, T. *Environ* **1993**, *33*, 281 553.
(61) Han, J. H.; S. T. Martin, *J. Geophys. Res.-Atmos* **1999**, *104*, 3543.
(62) Martin, S. T. *Chem. Rev.* **2000**, *100*, 3403.
(63) Martin, S. T.; Han, J. H.; Hung, H. M. *Geophys. Res. Lett.* **2001**, *28*, 2601.
(64) Onasch, T. B.; McGraw, R.; Imre, D. *J. Phys. Chem. A* **2000**, *104*, 10 797.
(65) Hanisch, F.; Crowley, J. N. *J. Phys. Chem. A* **2001**, *105*, 3096.
(66) Hanisch, F.; Crowley, J. N. *Phys. Chem. Chem. Phys.* **2001**, *3*, 2474.
(67) Chan, W. H.; Nordstrom, R. J.; Calvert, J. G.; Shaw, J. H.; *Environ. Sci. & Tech*, **1976**, *10*, 674.
(68) Cox, R. A. *J. Photochem*. **1984**, *25*, 43.
(69) Baulch, D. L.; Cox, R. A.; Crutzen, P. J.; Hampson, R. F.; Kerr, J. A.; Troe, J.; Watson, R. T. *J. Phys. Chem. Ref. Data* **1982**, *11*, 327.
(70) Appel, B. R.; Winer, A. M.; Tokiwa, Y.; Biermann, H. W. *Atmos. Environ*. **1990**, *3*, 611.
(71) Febo, A.; Perrino, C.; Allegrini, I. *Atmos. Environ.* **1996**, *30*, 611.
(72) Lee, Y. N.; Schwartz, S. E. *J. Geophys. Res.* **1981**, *86*, 11, 971.
(73) Kaiser, E. W.; Wu, C. H. *J. Phys. Chem*. **1977**, *81*, 1701.
(74) Sakamaki, F.; Hatakeyama, S.; Akimoto, H. *Inter. J. Chem. Kinet*. **1983**, *15*, 1013.
(75) Pitts, J. N., Jr.; Sanhueza, E.; Atkinson, R.; Carter, W. P. L.; Winer, A. M.; Harris, G. W.; Plum, C. N. *Int. J. Chem. Kinet.* **1984**, *16*, 919.
(76) Finlayson-Pitts, B. J.; Pitts, J. N., Jr. *Atmospheric Chemistry: Fundamentals; Experimental Techniques*; John Wiley & Sons: New York, 1986; p 540.
(77) Svensson, R.; Ljungstrom, E.; Lindqvist, O. *Atmos. Environ*. **1987**, *21*, 1529.
(78) Jenkin, M. E.; Cox, R. A.; Williams, D. J. *Atmos. Environ.* **1988**, *22*, 13, 487.
(79) Febo, A.; Perrino, C. *Atmos. Environ.* **1991**, *25A*, 1055.
(80) Junkermann, W.; Ibusuki, T. *Atmos. Environ* **1992**, *26A*, 17, 3099.
(81) Notholt, J.; Hjorth, J.; Raes, F. *Atmos. Environ.* **1992**, *26*, 211.
(82) Becker, K. H.; Kleffmann, J.; Kurtenbach, R. *J. Phys. Chem*. **1996**, *100*, 14 984.
(83) Harrison, R. M.; Peak, J. D.; Collins, G. M. *J. Geophys. Res. Atmos.* **1996**, *101*, 14 429.
(84) Lammel, G.; Cape, J. N. *Chem. Soc. Rev.* **1996**, 361.
(85) Kleffmann, J.; Becker, K. H.; Wiesen, P. *Atmos. Environ* **1998**, *32*, 16, 2721.
(86) Longfellow, C. A.; Ravishankara, A. R.; Hanson, O. R. *J. Geophys. Res*. **1999**, *104*, 13 833.
(87) Gerecke, A.; Thielmann, A.; Gutzwiller, L.; Rossi, M. *Geophys. Res. Lett*. **1998**, *25*, 2453.
(88) Kleffmann, J.; Becker, K.; Lackhoff, M.; Wiesen, P. *Phys. Chem. Chem. Phys*. **1999**, *1*, 5443.
(89) Kalberer, M.; Ammann, M.; Arens, F.; Gäggeler, H. M.; Baltensperger, U. *J. Geophys. Res.* **1999**, *104*, 13 825.
(90) Rogaski, C. A.; Golden, D. M.; Williams, L. R. *Geophys. Res. Lett*. **1997**, *24*, 381.
(91) Akhter, M. S.; Chughtai, A. R.; Smith, D. M. *J. Phys. Chem*. **1984**, *88*, 5334.
(92) Smith, D. M.; Welch, W. F.; Graham, S. M.; Chughtai, A. R.; Wicke, B. G.; Grady, K. A. *Appl. Spec*. **1988**, *42*, 674.
(93) Chughtai, A. R.; Welch, W. F.; JR.; Akhter, M. S.; Smith, D. M. *Appl. Spec*. **1990**, *44*, 294.
(94) Aumont, B.; Madronich, S.; Ammann, M.; Kalberer, M.; Baltensperger, U.; Hauglustaine, D.; Brocheton, F. *J. Geophys. Res.* **1999**, *104*, 1729.
(95) Stadler, D.; Rossi, M. J. *Phys. Chem. Chem. Phys.* **2000**, *2*, 5420.
(96) Alcala-Jornod, C.; van den Bergh H.; Rossi, M. J. *Phys. Chem. Chem. Phys.* **2000**, *2*, 5584.
(97) Arens, F.; Gutzwiller, L.; Baltensperger, U.; Gaggeler, H. W.; Ammann, M. *Environ. Sci.; Technology* **2001**, *35*, 2191.
(98) Kirchner, U.; Scheer, V.; Vogt, R. *J. Phys. Chem. A* **2000**, *104*, 8908.
(99) Saathoof, H.; Naumann, K. H.; Riemer, N.; Kamm, S.; Mohler, O.; Schurath, U.; Vogel, H.; Vogel, B.; *Geophys. Res. Lett*. **2001**, *28*, 1957.
(100) Masel, R. *Principles of Adsorption; Reaction on Solid Surfaces*; John Wiley & Sons: New York, 1996.
(101) Underwood, G. M.; Miller, T. M.; Grassian, V. H. *J. Phys. Chem. A* **1999**, *103*, 6184.
(102) Underwood, G. M.; Song, C. H.; Phadnis, M.; Carmichael; G. C.; Grassian V. H. *J. Geophys. Res.- Atmos.* **2001**, *106*, 18 055.
(103) Shimanouchi, T. *J. Phys. Chem. Ref. Data* **1977**, *6*, 1039.
(104) Leuchs, M.; Zundel, G. *J. Phys. Chem.* **1978**, *82*, 1632.
(105) Goodman, A. L.; Underwood, G. M.; Grassian, V. H. *J. Phys. Chem. A* **1999**, *103*, 7217.
(106) Jacox, M. E. *J. Phys. Chem. Ref. Data* **1990**, *19*, 1444.
(107) Barney, W. S.; Finlayson-Pitts, B. J. *J. Phys. Chem. A* **2000**, *104*, 171.
(108) Al-Abadleh, H. A.; Grassian, V. H. *J. Phys. Chem. A*, **2000**, *104*, 11 926.
(109) Saliba, N. A.; Mochida, M.; Finlayson-Pitts, *Geophys. Res. Lett.* **2000**, *27*, 3229.
(110) Fairbrother, D. H.; Sullivan, D. J. D.; Johnston, H. S. *J. Phys. Chem. A* **1997**, *101*, 7350.